Combinatorial investigation of Al—Cu intermetallics using small-scale mechanical testing

Yuan Xiao[1], *Hossein Besharatloo*[2], *Bin Gan*[3], *Xavier Maeder*[4], *Ralph Spolenak*[1], *Jeffrey M. Wheeler*[1]

[1]ETH Zurich, Department of Materials,
Laboratory for Nanometallurgy
Vladimir-Prelog-Weg 5, Zürich 8093, Switzerland
e-mail: yuan.xiao@mat.ethz.ch

[2]CIEFMA - Department of Materials Science and Metallurgical Engineering, EEBE, Universitat Politècnica de Catalunya-BarcelonaTech, 08019 Barcelona, Spain

[3]Beijing Key Laboratory of Advanced High Temperature Materials, Central Iron and Steel Research Institute, Beijing 100081, China

[4]Empa, Swiss Federal Laboratories for Materials Science and Technology,
Laboratory for Mechanics of Materials and Nanostructures
Feuerwerkerstrasse 39, Thun CH-3602, Switzerland

Abstract

In the past two decades, small-scale mechanical testing has become ubiquitous for mechanical measurements, offering new opportunities to quantitatively probe the mechanical behavior of materials. In this study, we applied four different small-scale mechanical testing techniques – conventional and statistical nanoindentation and micropillar compression and splitting tests – to study the mechanical behavior of Al—Cu intermetallics using a diffusion couple. This allowed the determination of the hardness, elastic modulus, yield stress, plastic flow behavior, and the critical stress intensity for fracture for nearly all of the intermetallic phases. A novel statistical indentation phase map plot was introduced, allowing the easy

visualization of phases within property space. Hardness and elastic modulus results were found to be in good agreement with more recent studies and DFT predictions, while fracture results suggest the single crystal forms of the intermetallics show superior toughness. This work demonstrates that using small-scale mechanical testing in a combinatorial manner allows the interrogation of intermetallics with large composition ranges in a high-throughput manner with high precision and efficiency.

Keywords: intermetallics; mechanical properties; diffusion; microstructure; phase diagrams

1. Introduction

Small-scale mechanical testing has progressed significantly since the advent of nanoindentation, the first automated technique to assess the local mechanical properties of materials at the nano- to micro-scale [1-3]. Particularly, the development of micro-compression testing by Uchic *et al.* [4], in conjunction with focused ion beam (FIB) specimen preparation, could be considered as a milestone in micro- to nano-mechanical testing. This subsequently enabled test geometries allowing compression, tension and bending at the sub-micron length scale [5]. These techniques are particularly effective for ascertaining the properties of phases/coatings/structures on the small-scale, which cannot be manufactured at a scale sufficient for more conventional large scale testing [6]. The small length scale of these methods also enables the rapid, combinatorial interrogation of relatively small composition gradients, such as those found in diffusion couples and welds.

For many industrial sectors, with the demand of increasingly complex designs in real applications, the welding of dissimilar materials is an indispensable technique. It does not only offer technical advantages, such as desired product properties, but also provides the benefits in terms of production economics [7]. Al—Cu joints are a good example, which are widely used in microelectronic packing applications, and could serve as an alternative to conventional aluminum-to-gold joints by virtue of the superior mechanical, electrical, and

thermal properties of copper [8, 9]. Such Al—Cu joints, usually made by friction stir welding, pressure welding, diffusion and roll bonding, flash welding and explosion welding, are characterized by a relatively stable joint interface and negligible volume fraction of intermetallics [10]. The formation of intermetallics is due to the incompatibility and the high diffusion affinity between Al and Cu at temperatures above 120 °C [11]. In general, intermetallics have good phase stability, corrosion resistance and high strength but very poor ductility and fracture toughness [12, 13]. For instance, the Al_2Cu intermetallic compound particles (Theta phase) have been used as reinforcing particles in metal matrix composites [14, 15]. Still, the structural application of Al—Cu joints has been limited due to uncertainty regarding the intermetallics´ mechanical behavior, since intermetallics can weaken the tensile, shear, and impact strengths of the joints [11]. The mechanical behavior of Al—Cu intermetallics has been previously evaluated (further discussed in Section 4.2) using several techniques: first principles calculations using density functional theory [9, 16], conventional microindentation [17-20], nanoindentation [21], conventional tensile and compression tests [17]. However, significant variation is seen between results from these studies, so significant uncertainty exists about the properties of individual Al—Cu intermetallics due to the difficulties in sample preparation and limitations of testing techniques [11].

To address this uncertainty, in this work, we employ four different small-scale mechanical testing methods to combinatorially evaluate the properties of the Al—Cu intermetallic phases. The first of these techniques is conventional nanoindentation. Several studies have also used nanoindentation of diffusion couples to directly investigate the properties of intermetallics phases in the Mg-Zn [22], Cu-Sn and Ni-Sn [23], and Au–Sn [24] systems. To examine the flow behavior of the intermetallics in the absence of the confining pressure of the indentation geometry, we next employ micropillar compression. This allows direct measurement of the uniaxial compressive failure and yield strength of the micro-scale intermetallic phases [25]. Lastly, to investigate the fracture behavior of the nominally brittle intermetallic phases, we

employ micro-pillar splitting. This allows us to more rapidly assess the fracture behavior in each phase than more complicated micro-geometries like micro-cantilevers, which were recently utilized to combinatorially investigate the composition- and crystal-structure-dependence of the fracture toughness of $NbCo_2$ Laves phases [26]. However, the use of FIB-machined sample geometries restricts the total number of samples which can be reasonably tested to a few selected grains in each phase, which currently limits the information which can be acquired about plastic and fracture anisotropy in complex intermetallic phases. Therefore, we also employ statistical nanoindentation using a high speed nanoindentation method, NanoBlitz, to ensure our results are valid for more than just a few grains of material. The results of these small-scale mechanical tests will then be summarized and compared with the existing literature.

2. Materials and Methods

2.1. Diffusion couple preparation

Cubic samples of pure alumnium (Purity: 99.999%) and oxygen-free copper (Purity: 99.99%) acquired from Alfa Aesar (Massachusetts, USA), with side lengths of ~1 cm, were lightly compressed at 350 °C for around 10 min in a vacuum environment using the Gleeble 3500 dynamic testing system to weld them together with a proper bond. After cooling to room temperature, the Al—Cu joint was encapsulated in an argon-purged quartz tube and then annealed at 500 ˚C for 312 hours (13 days), followed by a water quench. It is believed that the influence of residual stresses, as might result from quenching, on small-scale testing are quite small [27].

During the annealing, volume diffusion took place leading to solid solution and the formation of Kirkendall pores (Figure 1c) and intermetallic phases. The sample surface was prepared by conventional metallographic techniques: sectioned using an alumina cut-off wheel (Struers 50A 13), then polished using successively finer diamond abrasives finishing

with a 60 nm SiO_2 particle suspension. Afterwards, the sample was naturally aged at room temperature for several years. Before microstructural characterization and test geometry fabrication, the sample surface was polished by Ar^+ ion milling (IM4000, Hitachi, Japan) for 30 min to remove possible surface oxidation and damage layers. The microstructure and composition of the Al—Cu diffusion couple were characterized using electron backscatter diffraction (EBSD) technique and energy-dispersive X-ray spectroscopy (EDX) (EDAX, UK) using a scanning electron microscope (Lyra FIB-SEM, Tescan, Brno, Czech Republic). Beam conditions were 200 kV and 5 nA with the sample tilted at 70°.

2.2. Nanoindentation tests: *H*- *E*-mapping and statistical analysis

The *ex situ* nanoindentation measurements were made using an iNano nanoindenter (Nanomechanics, Inc, Oak Ridge, USA) using a diamond Berkovich indenter. This system uses a continuous stiffness measurement (CSM) technique, which measures the hardness from the stiffness measured via a small oscillation applied continuously during loading. A minimum of three indentation tests were performed on each Al—Cu intermetallic phase.

A high-speed mechanical property mapping technique, NanoBlitz, wherein each test takes less than 1 second - which includes positioning the testing region under the tip, surface approach, loading, unloading and retracting. This novel fast testing technique offers indentation property mapping over relatively large areas through arrays consisting of thousands of indentations, each assessed by the Oliver and Pharr method [28, 29]. Five large indentation maps (~12,000 indents in total) were conducted in different areas of the Al—Cu intermetallic region of the diffusion couple for statistical analysis at a maximum load of 15 mN. On the one hand, a larger indentation density improves the resolution and accuracy of indentation hardness and elastic modulus maps, moreover it also supplies greater numbers of indentations for statistical analysis. On the other hand, indentation spacing is a critical parameter, which has to be taken into account in order to avoid any overlapping effect of

neighboring indentations. Indentations were spaced at an interval of 5 µm to ensure the suggested indentation depth/spacing ratio of 10 was maintained [30] .

2.3. Micropillar fabrication

For *in situ* micropillar compression tests, pillars were fabricated with a target diameter of ~1 µm and an aspect ratio of ~3 at an accelerating voltage of 30 kV using a Ga^+ focused ion beam (FIB) system (Helios 600i, Thermofischer Scientific). A two-step milling method was employed with milling currents of 0.79 nA for coarse milling and 24 pA for fine polishing. A minimum of four pillars were produced within single grains of each individual intermetallic phase, previously identified using EBSD mapping. For *in situ* splitting tests, pillars with diameter of ~10 µm and an aspect ratio of ~1 were FIB machined, to minimize the influence of FIB damage on toughness [31]. Initially, probe current of 9.7 nA was used to mill the rough pillar shapes and 40 pA was used for the final polishing to obtain smooth surfaces and to remove the possible Ga damage layer [32]. Micropillars for compression and splitting tests were produced from single grains for each intermetallic phase, except for in the Zeta phase due to smaller grains. The morphologies of the pillars were characterized using a high-resolution SEM (Magellan, Thermofischer Scientific) before and after micro-mechanical testing.

2.4. Micropillar compression and splitting tests

Micropillar compression testing was performed using an *in situ* Indenter system (Alemnis AG, Thun, Switzerland) inside a Vega 3 (Tescan, Brno, Czech Republic) SEM [33]. A diamond flat punch tip with a 3 µm diameter was used. All pillars were compressed at a constant displacement rate of $2\times10^{-3}\,s^{-1}$ to ~10% strain. The engineering stress was calculated using the top surface of the pillar, and the yield strength (the stress at which the pillar begins to deform plastically) was determined from the onset of general yielding to evaluate the mechanical properties.

All pillar indentation splitting tests were carried out using the same testing system as used for the micropillar compression tests. A diamond cube corner indenter was used to perform the splitting at a speed of 0.1 μm/s in the displacement control mode. The critical stress intensity for fracture, K_c, was determined from the relationship:

K —— (3),

where C is a dimensionless coefficient between 0 and 1 determined by finite element analysis from the material's elastoplastic properties, P_c the critical load at failure, and R the radius of the pillar [34]. The ratios of the elastic modulus to the hardness (E/H) of individual phases obtained from our nanoindentation tests were used to calculate the correct value of C for each phase using the relationships Ghidelli *et al*. [35] determined for pillar splitting using a cube corner indenter.

3. Results

3.1. Phase analysis

The phase diagram of the Al—Cu system has been previously studied in great detail. A summary of the Al—Cu intermetallic phases expected [36] in the diffusion couple after quenching from 500˚C is presented in Table 1 and Figure 1a. To determine the lateral spacing of these phases within the diffusion couple, energy-dispersive X-ray spectroscopy (EDX) elemental composition analysis of the intermetallic phases and the corresponding back-scattered electron (BSE) micrograph was performed - Figure 1b and 1c respectively. All five low temperature phases in the Al—Cu phase diagram were identified within the interdiffusion zone, namely γ_1, δ, ζ_2, η_2, and θ. Small compositional gradients are still observed within each phase, which are larger than their ambient temperature literature values as a consequence of the quenching from 500 °C shown in Figure 1a. The compositional ranges observed in the intermetallics instead correspond to their higher temperature stoichiometry ranges on the phase diagram. From the BSE micrograph in Figure 1c, it is difficult to determine the phase

boundaries between the δ and γ_1 phases due to the lack of contrast, which was also the case in [20]. By combining EDX measurements and Table 1, the δ and γ_1 phases were identified for subsequent micromechanical testing micropillar fabrication. The order and phase widths of all phases are consistent with findings of Funamiza and Watanabe [37].

Stoichiometry	Name	Symbol	Crystal Structure	Composition Range (at.-% Cu)
Cu	Alpha	α_{Cu}	Face-Centered Cubic	>80.31
Cu_9Al_4	Gamma 1	γ_1	A12 Cubic	59.8-70
Cu_3Al_2	Delta	δ	A7 Rhombohedral	59.3-61.9
Cu_4Al_3	Zeta 2	ζ_2	Body-Centered Orthorhombic	55.2-56.3
CuAl	Eta 2	η_2	Monoclinic	49.8-52.3
$CuAl_2$	Theta	θ	Body-centered Tetragonal	31.9-33.0
Al	Alpha	α_{Al}	Face-centered Cubic	0-2.48

Table 1: Summary of the nomenclature, structure and compositional ranges of the Al—Cu intermetallic phases in the diffusion couple, as suggested by Murray [36].

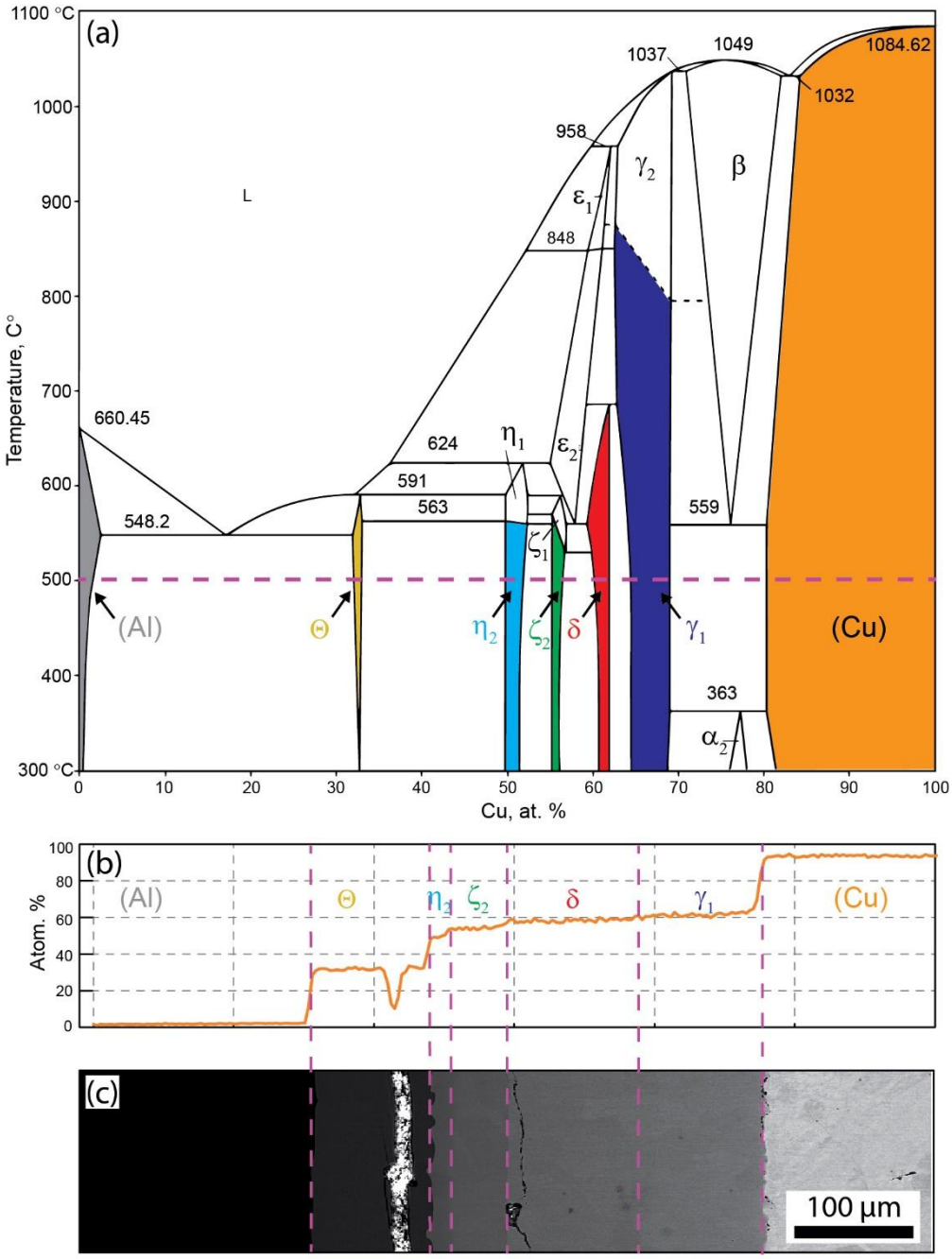

Figure 1: Phase analysis of the Al—Cu couple: (a) Al—Cu phase diagram [36] with investigated intermetallic phases indicated; (b) the copper concentration profile measured by EDX and (c) a BSE micrograph showing a crack in the Theta phase illuminated by silver paint.

3.2. Indentation

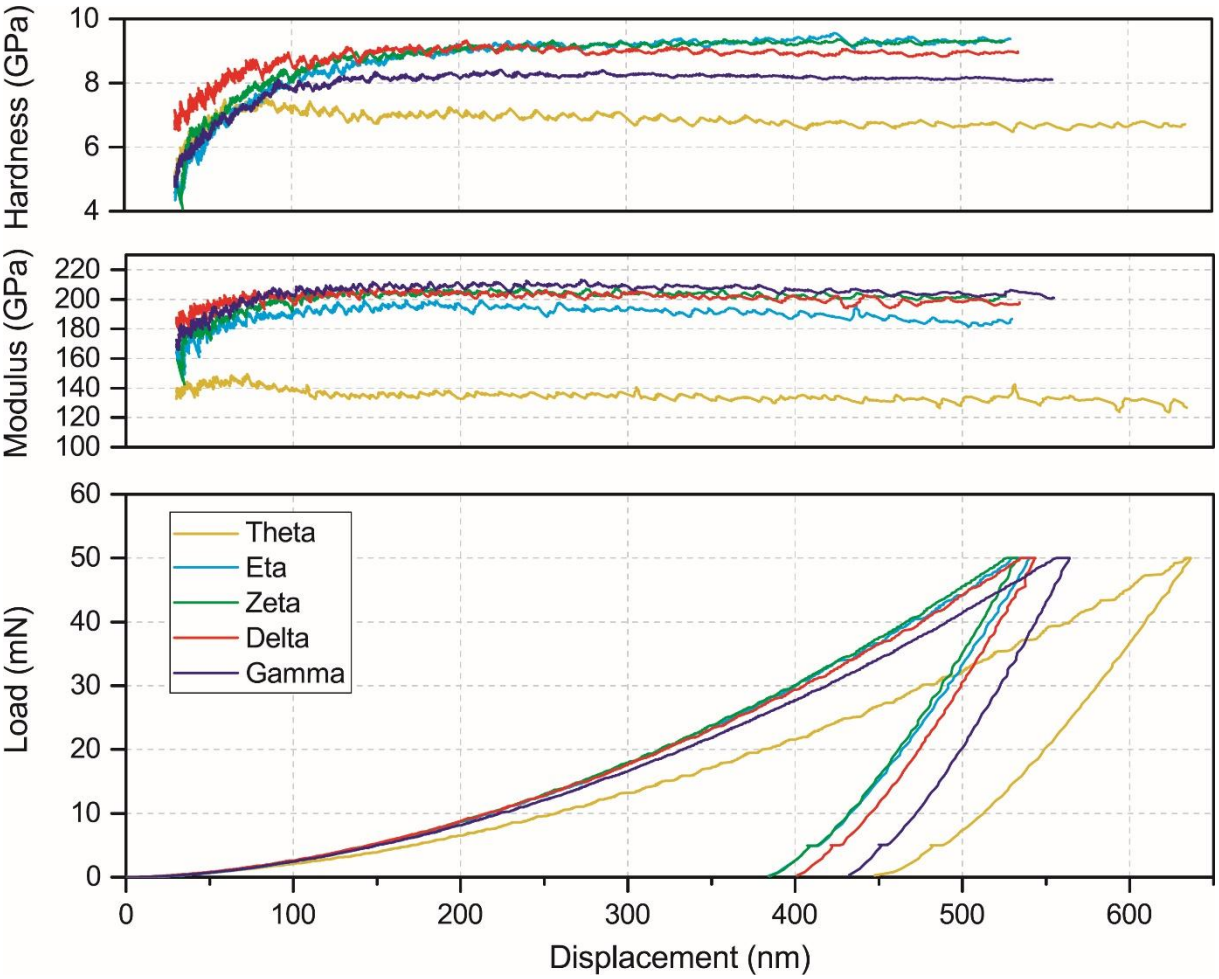

Figure 2: Representative load-displacement and hardness and modulus values from indentation tests of Theta, eta, Zeta, Delta and Gamma phases using a Berkovich indenter at a maximum load of 50 mN.

After the identification of the zones for each phase by EDX, conventional nanoindentation testing was applied to determine the hardness and modulus of each of the Al—Cu intermetallic phases. Figure 2 displays the applied load, and measured hardness and modulus curves as a function of displacement into the surface for Theta, Eta, Zeta, Delta and Gamma phases, obtained from indentation data. It can be seen that the Eta and Zeta phases show the highest hardness and modulus values, while the Theta phase displays the lowest values. However, the differences between hardness values for the Eta, Zeta and Delta phases appear rather small, as do the modulus values of the Zeta, Delta, and Gamma phases. Moreover, it can be seen that *H* and *E* curves for all the phases are discerned to follow trends towards plateau level when the penetration depth exceeds 150 nm. Therefore, it demonstrates that

obtained mechanical properties of these phases are not dominated by any indentation size effect (ISE) for penetration depths greater than 150 nm [38].

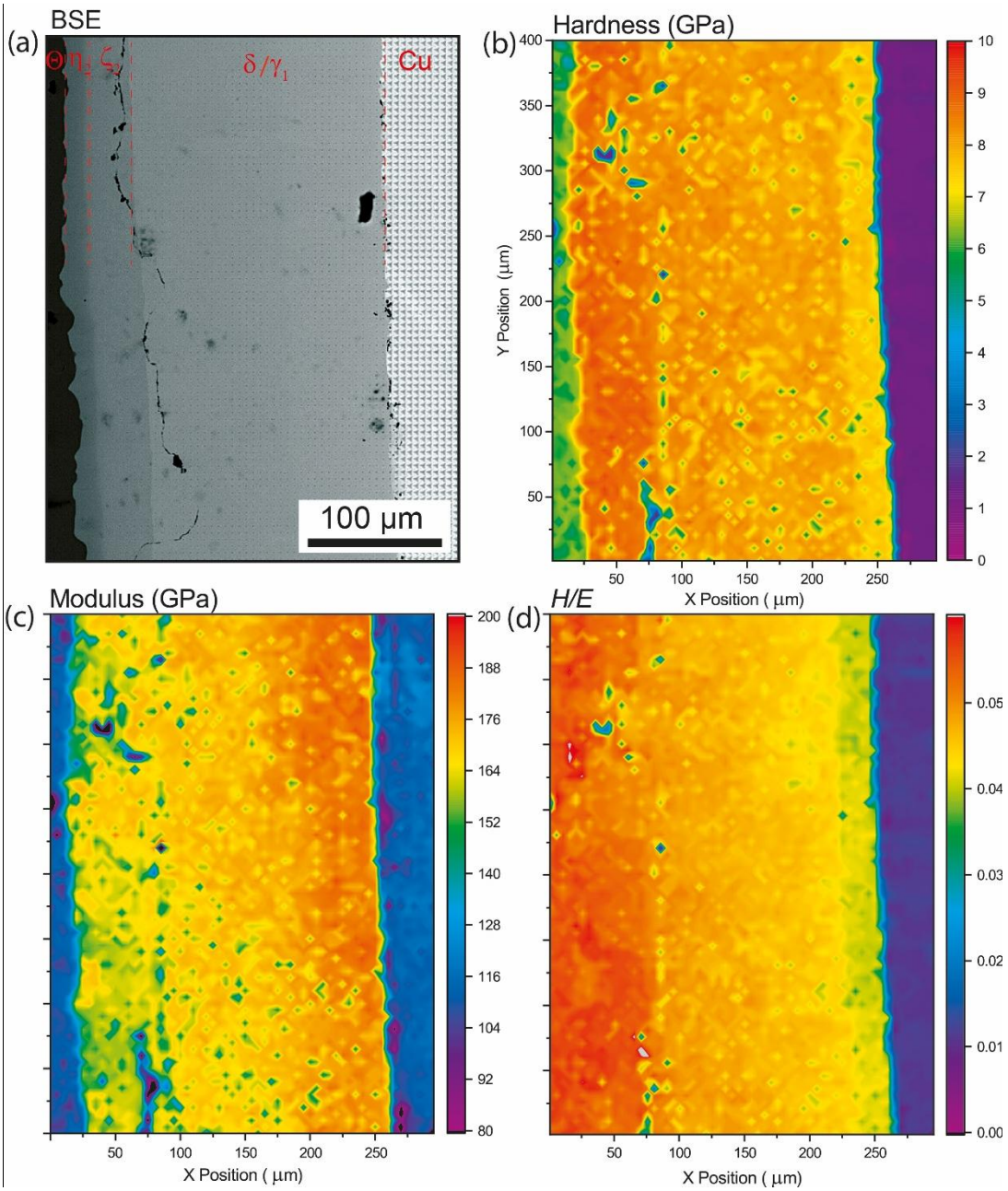

Figure 3: Indentation map of an Al—Cu intermetallic region with an area of 300×400 µm (~5,000 indents): (a) BSE after indentation, (b) hardness, (c) modulus, and (d) H/E maps.

After conventional indentation testing was performed to determine a first estimate of the values for each phase and to determine the appropriate load to achieve a representative depth, indentation mapping was performed using the NanoBlitz module to statistically evaluate the mechanical properties. Rather than one large single map, several maps were performed in different locations along the couple to avoid existing conventional indentations, and areas where EBSD and micromechanical testing were performed. Figure 3 shows a BSE micrograph

of one of the mapped areas after indentation and the resulting extracted hardness, modulus and *H/E* ratio maps from the ~5000 indentations performed in this area. The Theta, Eta, Zeta and copper phases can be easily differentiated in the BSE image (the spot contrast in Figure 3a is due to the indents), while Delta and Gamma are less distinct. Local drops in hardness and modulus can be seen to correlate to porosity at the Matano interface (porosity at the initial location of the surface of the Al and Cu prior to diffusion) and possibly additional subsurface porosity. The Young´s modulus and the hardness maps have similar appearances but with a slightly higher variation in modulus values as compared to the hardness values within the Eta and Zeta region - Figures 3b & 3c. In general, it is clear that the indentation mapping results are consistent with electron microscopy and exhibit values which are consistent with those from the conventional indentation values of each of the intermetallic phases shown in Figure 2.

3.3. Micro-pillar compression

To further investigate the mechanical behavior of the intermetallic phases under uniaxial straining, micro-pillar compression tests were performed within single grains of the intermetallic phases. Characteristic stress-strain curves of Theta, Zeta, Delta and Gamma phases are shown in Figure 4a (Eta is not included due to the crack occurred shown in Figure 1b). Generally, intermetallic phases are very hard and brittle at room temperature, and show little ductility during deformation in bulk tests. However, in this study, all brittle intermetallic phases demonstrate significant plasticity during micro-scale testing. This results from a well-known size-induced brittle-to-ductile transition in brittle materials [39], which has been previously observed in semiconductor materials such as silicon [40, 41] and even quasicrystals [42].

It is interesting to observe the serrated stress-strain curves during the deformation of Zeta and Theta phases. Similar serration behavior has also been seen in the deformation of Fe_7Mo_6 and Mg_2Ca intermetallics [43, 44]. In the case of Eta and Theta phases, the dislocation

mobility is very limited due to their low symmetry crystal structures: body-centered orthorhombic for Zeta and body-centered tetragonal for Theta. Such structures only allow dislocation motion on relatively few slip systems, as observed in Figure 4b. Similar serrated behavior is also observed in the conventional nanoindentation load-displacement curves in Figure 2 as pop-ins or displacement bursts, due to the system's load-controlled operation.

In contrast to the large load drops observed in the stress-strain curves of Zeta and Theta phases, the slightly intermittent plastic flows of Delta and Gamma phases (rhombohedral and cubic crystalline structure, respectively) are believed to be associated more with dislocation avalanches, where the dislocations nucleate from a single, or very few, dislocation sources then pile-up at the pillar surface before escaping and annihilating – intermittently causing stress increases and then sharp decreases [45]. Gamma and Delta apparently have near metallic mobility and ductility, where the dislocation motion can easily occur and lead to plastic deformation. Both Delta and Gamma phases also exhibit apparent work hardening behavior, indicating dislocation-dislocation interactions and possible interaction from non-parallel slip planes leading to multiple slips observed in Figure 4b.

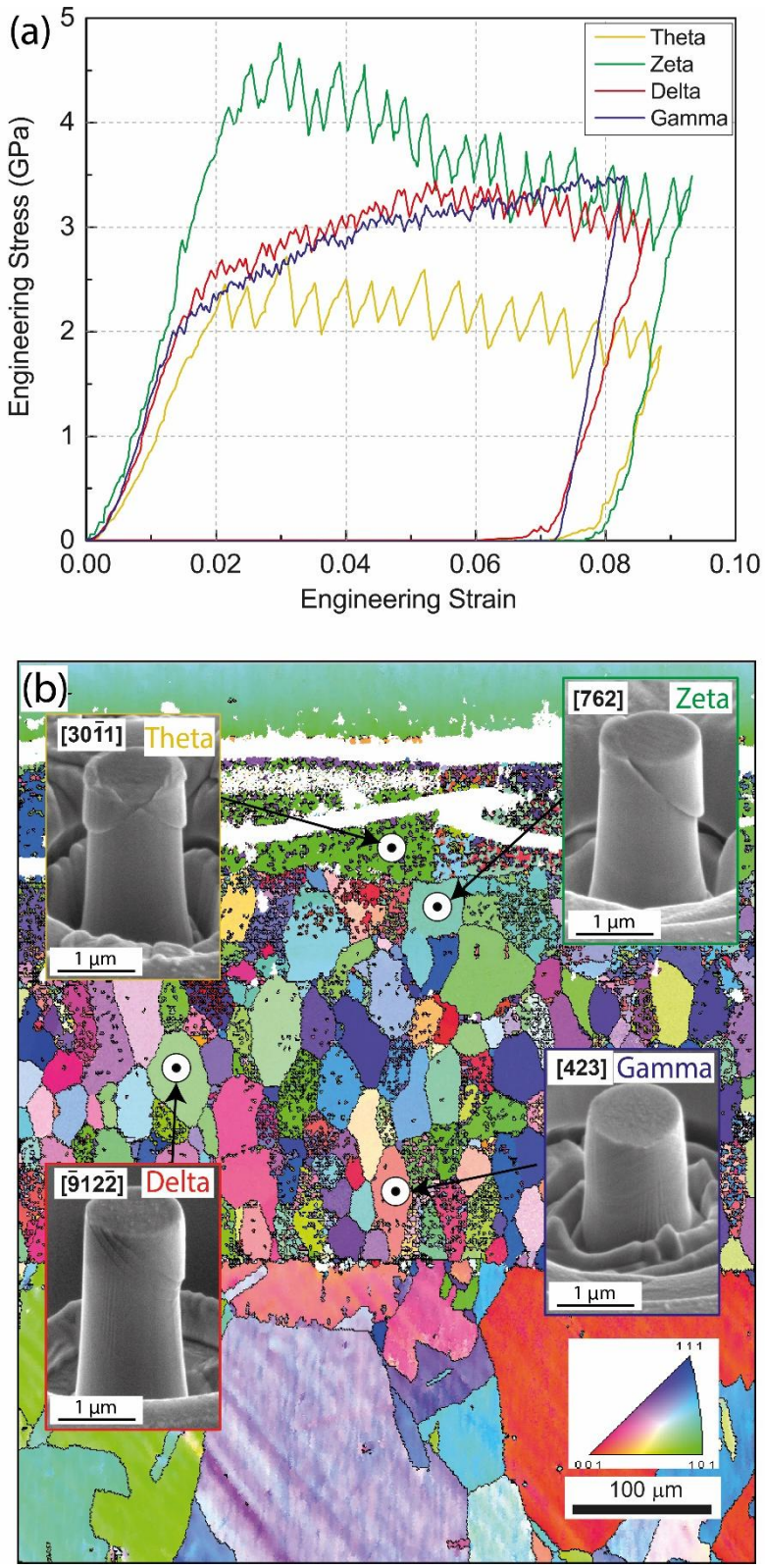

Figure 4: (a) Representative stress-strain curves of Zeta, Delta, Theta and Gamma from micro-pillar compression tests (Variation between tests in each case was significantly less than the differences shown between representative curves shown.), and (b) the corresponding SEM images of the deformed pillars with the Miller Indices on the upper left and their positions in the EBSD orientation map.

SE micrographs of the deformed pillars with the Miller Indices on the upper left and their corresponding positions on the EBSD orientation map are presented in Figure 4b. It has to be

mentioned that the Miller Indices for the grains are obtained assuming the crystal structures to be face-centered cubic. To understand the possible mechanisms that might cause the variations of the stress-strain curves, it is instructive to examine the deformation morphologies of the pillars. A few large slip offsets are observed in the Zeta and Theta pillars, indicating relatively few dislocation sources and slip systems could be activated [43]. However, a larger number of smaller slip traces are observed along the Delta and Gamma pillars, similar to previously observed slip behavior of cubic metals [4]. These slip offsets or slip lines indicate the activated slip systems in crystals and are found to be oriented at approximately 45° from the loading axis, which is believed to relate to their slip planes. For the tetragonal Theta phase, the operative slip systems in single crystals have been previously studied at bulk scale [12, 13, 46]. Three independent slip systems of), and are reported for using molecular dynamics method [47]. The slip on the plane in the Theta phase is observed to cause the decomposition within the slip plane [47], which probably explains the ragged edges observed on the slip lines shown in Figure 4b.

3.4. Micro-pillar splitting

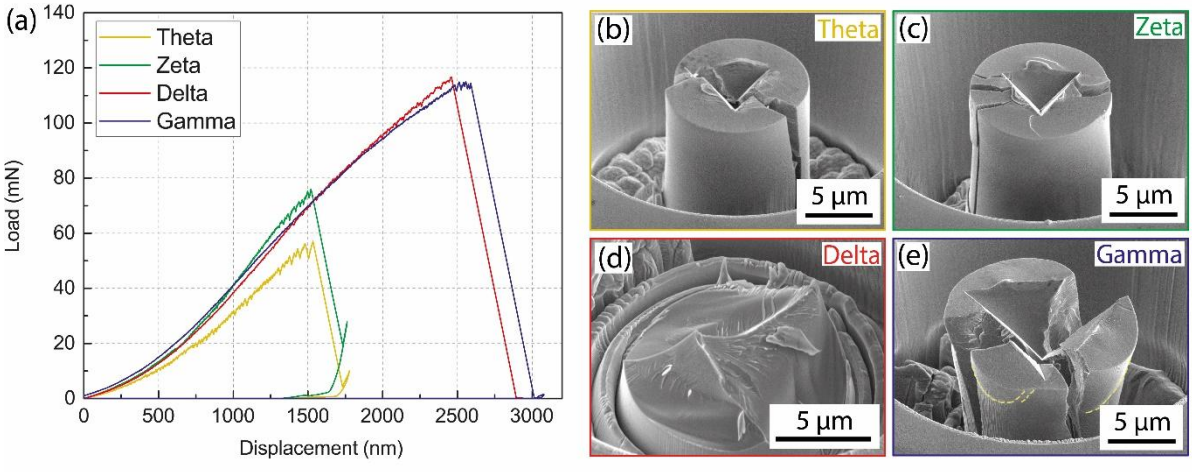

Figure 5: (a) Representative load-displacement curves and (b-e) SEM images of the different failure morphologies observed of Delta, Gamma, Zeta and Theta phases.

Although Al—Cu intermetallics have been studied since a long time, our knowledge about the fracture behavior of each phase is still quite limited due to the difficulty and cost of producing sufficiently large samples for conventional mechanical tests. So far, it is reported

that the phenomenon of the transformation of fracture mechanism is dominated by the interfacial structures in Al—Cu joints [48]. In this study, we implemented the indentation pillar splitting test, developed by Sebastiani *et al.* [49] to measure toughness of brittle materials [31, 50], to investigate the fracture behavior of the individual Al—Cu intermetallic phases. Due to the narrow width of Eta phase (Figure 1), which limited the pillar size for splitting test in the area of interest, we focused on the fracture behavior of Theta, Zeta, Delta, and Gamma phases. Figure 5 shows the representative load-displacement curves of Theta, Zeta, Delta, and Gamma phases tested at room temperature and the corresponding SE micrographs of the fractured pillars. Since indentation was performed under displacement control, load drops (shown in Figure 5a) occurred in the load-displacement curve when the pillars fractured, rather than the catastrophic pop-in behavior usually seen under the load control.

In Figure 5, all the pillars were fractured by indentation splitting tests. A clear maximum load is observed according to the load drop shown in Figure 5a, which allows simple quantification of the critical load at failure. Zeta and Theta pillars have a lower critical load than that of Delta and Gamma pillars, which agrees well with the general trend of higher strength – lower toughness (Figure 4a). In real application, Eta, Zeta and Theta phases are also observed to be more sensitive to fracture than Gamma and Delta phases [11, 16, 20, 48] due to the difficulties in nucleating dislocations and the low initial dislocation density [11].

Different crack morphologies were seen for several of the phases shown in Figure 5 (b-e). In the Delta and Gamma phases, the pillars fractured by 3-way splitting, where three cracks starting from each corner of the indenter nucleate during indentation and suddenly propagate to the edges of the pillar at the critical load. However, in the harder phases, both the Zeta and Theta phase pillars fractured by cleavage, ignoring the stress concentration of the indenter corners, suggesting a crystallographic direction of easy crack propagation and significant fracture anisotropy. The Gamma pillar (Figure 5e) shows a pronounced localized plastic zone

at the top of the pillar, while the fracture surface of Delta phase (Figure 5b) exhibits a quasi-cleavage feature with slightly river markings. Cleavage fracture in the Theta phase has been previously reported using bulk three point bending tests at room temperature [51] and results from crack propagation initiating and extending along the (001) cleavage plane.

4. Discussion

4.1. Statistical indentation analysis

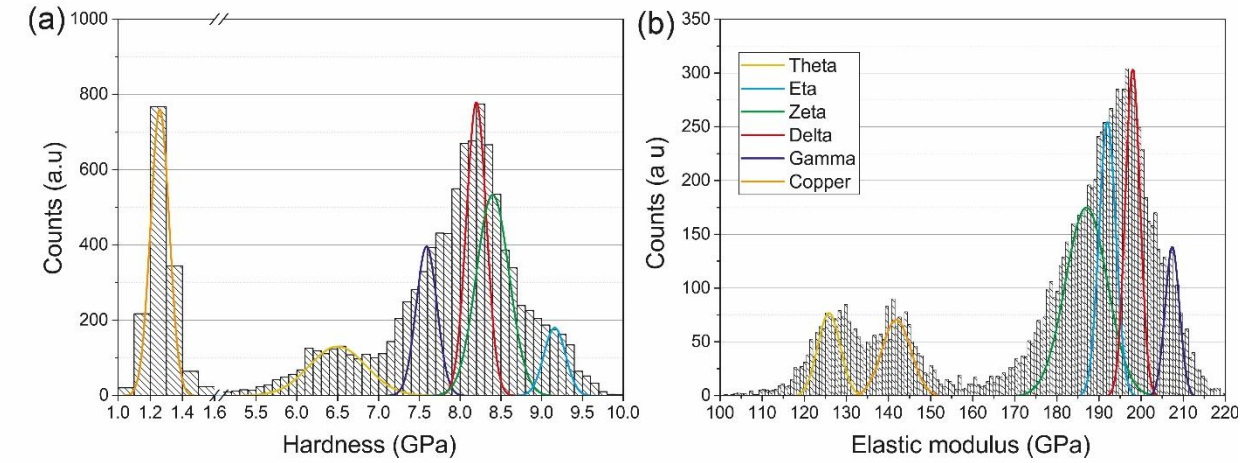

Figure 6: (a)Hardness and (b) elastic modulus histograms for Al—Cu intermetallic phases, as well as copper, determined from 12,000 indents performed to maximum applied load of 15 mN.

Since the variation between conventional nanoindentation results was quite small for several phases (Figure 2), and micropillar testing is limited to a relatively small number of grains with different crystallographic orientations; statistical sampling of the intermetallic phases with hundreds of interrogated grains was performed using the NanoBlitz indentation mapping technique. The statistical method employed to assess the *H* and *E* response of each intermetallic phase in the Al—Cu diffusion couple was first proposed by Ulm and co-workers [52-55]. In this method, the investigated sample were considered to contain various (i) constitutive phases, which are chemically and mechanically distinct [53-56]. In this regard, six different phases were considered for the investigated sample: copper, Theta, Gamma, Delta, Eta and Zeta. The aluminum side of the couple was excluded due to a fracture in the Theta phase positioning the two sides of the couple at different heights, precluding safe indentation

mapping over the area. The Ulm method assumes that the distribution of mechanical properties (P_i) of each phase follows a Gaussian distribution:

$$P_i = \frac{1}{\sqrt{2\pi\sigma_i^2}} \exp\left[-\frac{(P-P_i)^2}{2\sigma_i^2}\right] \quad (1),$$

where σ_i is the standard deviation and P_i is the arithmetic mean (H or E) for number of indentations exerted on different constitutive phases (i). P values were plotted by cumulative distribution function (CDF), while density functions were fitted by Gaussian distributions. Therefore, the corresponding CDF using a sigmoidal shaped error function may be fitted by following equation:

$$CDF = \sum_i^n \frac{1}{2} \cdot f_i \cdot erf\left[\frac{P-P_i}{\sqrt{2}\sigma_i}\right] \quad (2),$$

where f_i corresponds to the relative function occupied by each individual phases. The fitting process was considered to be successful when a χ^2 tolerance of less than 1×10^{-15} was achieved. The total volume fraction of constitutive phases was fixed at 1.

Figure 6 shows hardness and elastic modulus histograms for Theta, copper, Zeta, eta, Delta and Gamma phases generated from 12,000 indents using the CDF analysis. We were able to successfully extract the hardness and elastic modulus values for each phase from the peak analysis of the CDFs. These values are compared to values from the literature and the other employed micromechanical investigation techniques in the following section.

In the employed statistical analysis, hardness and elastic modulus are considered separately. However, in reality, these two properties are closely interrelated for each phase and share similar anisotropy due to their parent crystal structure. A novel way to examine these properties together for phase identification and analysis is presented in Figure 7, which displays the values from the ~12,000 indents performed as a 2D histogram map of hardness vs elastic modulus, which each shaded "pixel" represents the number of indentations contained within the 2D bin within a range of hardness and modulus. Darker shaded bins correspond to a greater number of indents contained within the bin. This produces a "heat

map" where darker regions correspond to 2D histogram peaks. In appearance, this statistical indentation phase map is similar to an Ashby property map [57] and allows phases to be grouped by intensity. As with all statistical methods, the accuracy and clarity of this indentation phase map improves with the increasing sample numbers.

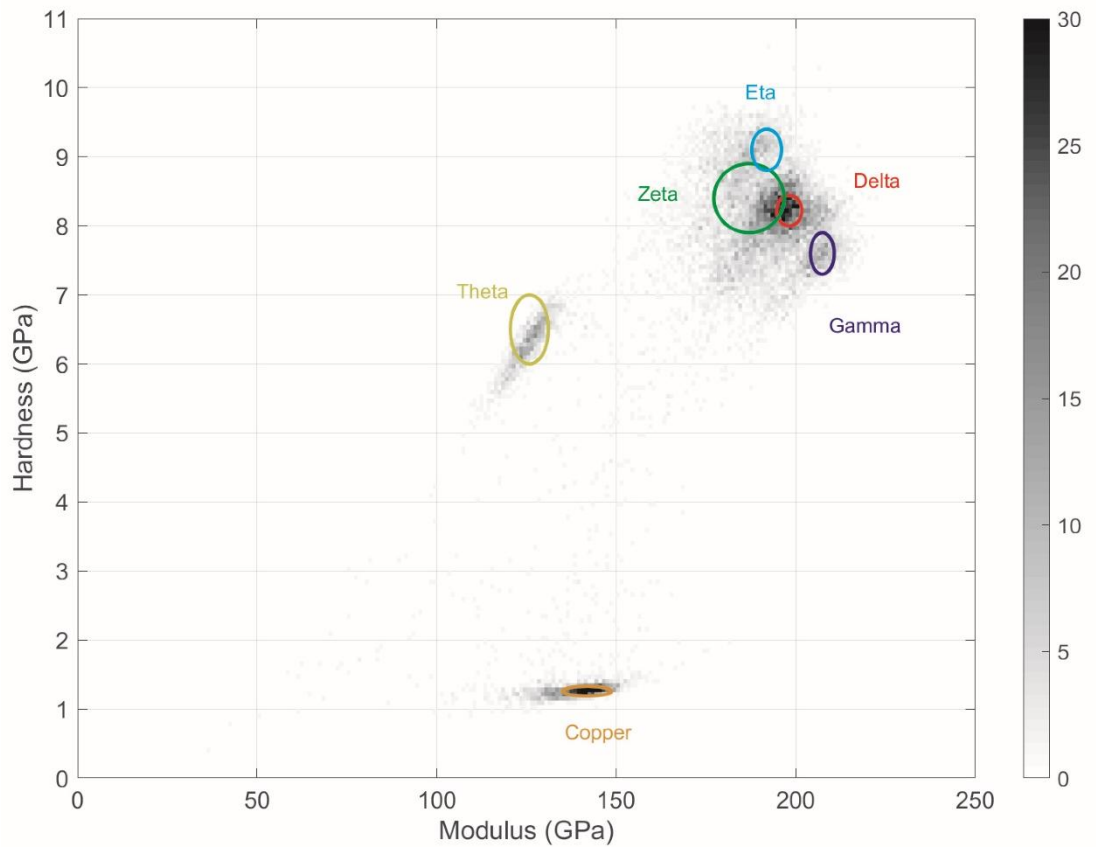

Figure 7: Statistical indentation phase map of the Al—Cu intermetallic region: 2D histogram of hardness versus modulus extracted from ~12,000 indents with ellipses labeling each phases' H and E values with errors as obtained from the conventional statistical analysis.

Several interesting features emerge from a map of this type. Porosity or roughness causes streaks or trails of the phase peak in the direction of the origin along the slope of their *H/E* ratio, as indents into porosity represent a composite of the phase and a void. Adjacent phases produce streaks between their peaks, as several indentations which overlap both phases produce composite values of the two neighboring phases. Isotropic phases would show perfectly circular or elliptical distributions, whereas anisotropic phases show skewed peaks with a slope aligned with their *H*/*E* ratio. An example of this can be seen in the copper phase, where the peak is significantly more elongated on its modulus axis compared to its hardness axis – indicating greater elastic anisotropy compared to relatively isotropic plasticity. Some

phases in Figure 7, such as copper and Theta, can be clearly distinguished due to their significantly different properties from the other phases, while it is harder to distinguish the peaks for the Delta, Eta and Zeta phases due to overlapping properties. Using the results from the statistical analysis employed in Figure 6, the *H* and *E* values for each phase are plotted in Figure 7 as ellipses centered on the mean values with axis lengths scaled to the standard deviation of the fitted peaks. Good agreement can be seen between these elliptical labels assessed by the statistical analysis and the peaks seen in the 2D histogram. The relatively large ellipse of the Zeta phase is due to its higher standard deviations, which are due either to high anisotropy, insufficient number of indentations or to local porosity in the phase.

It is not surprising that significant anisotropy can be observed in the Al—Cu intermetallics' mechanical properties, which have been reported to be strongly dependent on crystallographic orientation [16]. This anisotropy is most pronounced in Figure 7 in the Theta and copper phases, as manifested by their elongated shapes and wide scattering in modulus histogram. In industrial applications, this anisotropy is important for Al—Cu joints, since it has an influence on the electronic nature of Al—Cu intermetallic compounds [9]. However, since a three-sided Berkovich indenter is used, and the indentation properties are extracted from multi-axial expanding cavities for the plastic and elastic zones; it is expected that the observed anisotropy is far less than the actual values [58]. Therefore, this type of mapping can currently only provide qualitative indicator of anisotropy, rather than quantitative values. Future work using alternative indenter geometries may be able to improve upon this.

4.2. Mechanical properties overview and literature comparison

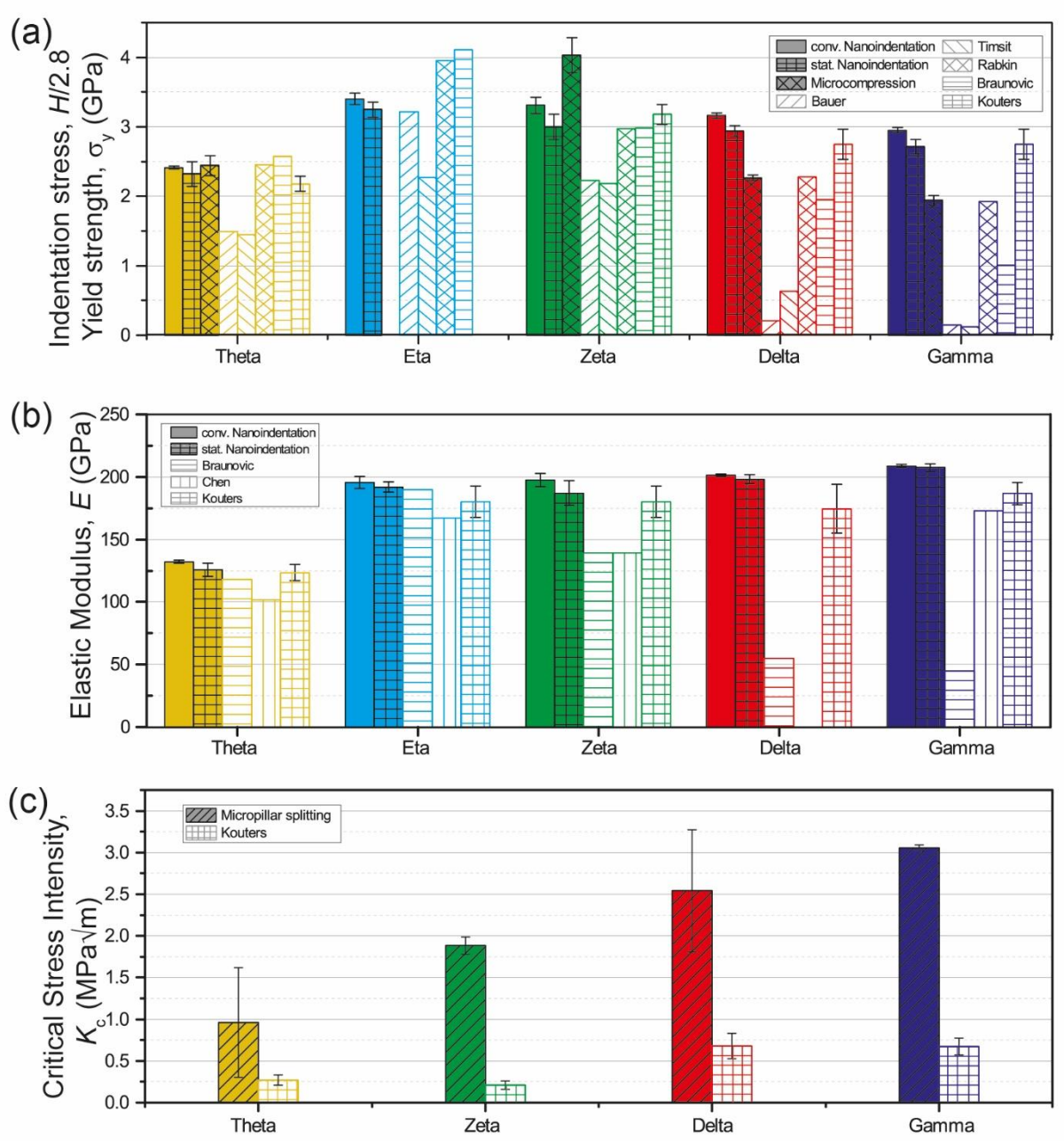

Figure 8: Mechanical properties of the Al—Cu intermetallics and copper phase in comparison with literature values [16-21]: (a) indentation stress (H/2.8) and the micro-pillar yield strength, (b) elastic modulus, and (c) critical stress intensity from micro-pillar splitting and from Palmqvist indentation toughness [20].

As several different methods were employed to characterize the mechanical properties of the intermetallic junction of the phase diagram, a comparison of the various methods is warranted. This is provided in Figure 8 along with literature values for additional comparison. Figure 8a-b illustrates the indentation stress, micropillar yield stress, and elastic modulus values from conventional and statistical nanoindentation testing in comparison with literature

nano- and micro-indentation values [16-21]. For comparison with uniaxial microcompression yield stress values, the hardness values were converted into representative indentation stress values by dividing them by a confinement parameter of 2.8 [59]. The yield strength, the stress at which the pillar begins to deform plastically, was determined from the onset of general yielding to account for variation in work hardening and scatter from serrated flow. It can be seen that our statistical nanoindentation values fall between the conventional nanoindentation and micropillar values, which indicates they represent the average properties over a large area. The indentation stress and evaluated *E* from both conventional and statistical nanoindentation from the current work match well with the recent nanoindentation values from Kouters *et al*. [20] as well as DFT calculations of *E* from Chen *et al.* [16]. Slightly higher variations in stresses and *E* values are observed from Braunovic *et al*. [21], who reported lower values for many phases. It seems that lower values for the intermetallic phases are obtained using micro-Vickers testing reported by Bauer *et al*. [18] and Timsit *et al*. [19], possibly due to the influence of cracking. The scatter in the reported values for both *H* and *E* values could be related to testing and/or manufacturing methods, moreover anisotropy of studied samples may have a significant influence on measured values [9], which was mentioned in last section.

If we compare these indentation stress values to the uniaxial yield strength values from micropillar compression, Figure 8a, we can see that the indentation stresses/yield strengths of intermetallic phases are one order of magnitude greater than that of pure copper phase, which indicates good agreement between the micropillar and nanoindentation tests. However, within the intermetallic phases, we can see some significant differences between the values from micropillar compression and nanoindentation. This is possibly due to anisotropy between the few selected grain orientations used for micropillar compression and the averaged values from numerous grains in statistical nanoindentation. Since microcompression allows targeting of individual slip systems, it is possible that weaker or stronger slip systems were inadvertently

targeted relative to the overall response given by indentation testing, which activates all possible slip systems.

Considering the fracture behavior of the intermetallics, the calculated critical stress intensities, K_C, for Theta, Zeta, Delta and Gamma phases are plotted in Figure 8c. All these intermetallic phases exhibit critical stress intensity values within a similar magnitude, 1.4-3.1 MPa√m, indicating the expected brittle behavior. However, our pillar splitting values are ~ 4× higher than those estimated from Palmqvist measurements from indentation cracking [20]. While both techniques are subject to some sources of error, e.g. FIB damage or tip blunting effects on pillar splitting and crack shape uncertainty for indentation cracking, in general the primary difference between these techniques is the scale. Indentation cracking methods required high loads using a Vickers indenter to achieve fracture in many cases [20], which suggests that these values may represent more bulk fracture behavior with effects from grain boundaries and porosity. In this case, the micropillar splitting tests can be considered to be more representative of single crystalline behavior. However, the 3-sided indenter geometry precludes the investigation of anisotropy for most 4-fold cubic orientations. Previous results using micropillar splitting within a similar range of toughness have been validated against bulk test methods and found to be in good agreement with bulk values: ~0.7 MPa√m for (100) silicon in [31, 60] and 2-4.5 MPa√m [35, 50]. Therefore, the values seen for the studied intermetallic phases falls between the validated range for the technique. However, the two-way cleavage fracture observed for the Theta and Zeta phases was also previously observed in pillar splitting of silicon at elevated temperatures [31], where it coincided with a 20-30% overestimation of the critical stress intensity due to excessive plasticity underneath the indentation. This suggests that the critical stress intensity values for these phases may be similarly overestimated, and highlights the limitations of applying a three-fold symmetry indenter to probe anisotropic fracture in intermetallics. Though, higher values of fracture toughness in the range of 4.5-6.2 MPa√m have been observed in bulk three-point bending of

Theta-based alloys due to extra toughening from the eutectic lamellar phases [51], we would suggest the actual, single-crystalline values of toughness may lie between our values and Kouters.

5. Summary

In this work, we successfully applied four different small-scale mechanical testing techniques on a diffusion couple sample to combinatorially investigate the mechanical behavior of Al—Cu intermetallics. These techniques included conventional and statistical nanoindentation as well as micro-pillar compression and splitting tests. This enabled us to determine the hardness, elastic modulus, yield stress, plastic flow behavior, and the critical stress intensity for fracture for nearly all of the intermetallic phases. Hardness and elastic modulus results were found to be in good agreement with more recent studies and DFT predictions, while fracture results suggest the single crystal forms of the intermetallic phases, frequently used for precipitate strengthening of aluminum alloys, show superior toughness. A novel, statistical indentation phase map plot was introduced, allowing the easy visualization of phases within property space. The distribution shapes of different phases are particularly sensitive to anisotropy; isotropic phases appear as circular or elliptical distributions, whereas anisotropic phases display skewed distributions with a slope aligned with their *H/E* ratio. The high-throughput, small-scale testing techniques demonstrated in this work illustrate the power of the combinatorial approach to materials investigation and offer new opportunities for the rapid evaluation of the mechanical behavior of materials.

Acknowledgements

The authors would like to thank C. Zaubitzer (ScopeM, ETH Zurich) for his help in the sample preparation using FIB. B. Gan would like to gratefully acknowledge the financial support of the project from the National Natural Science Foundation of China (No. 51601147).

Disclosure statement

No potential conflict of interest was reported by the authors.

References

[1] J.B. Pethicai, R. Hutchings, W.C. Oliver, Hardness measurement at penetration depths as small as 20 nm, Philosophical Magazine A, 48 (2006) 593-606. doi: 10.1080/01418618308234914.

[2] G. Dehm, B.N. Jaya, R. Raghavan, C. Kirchlechner, Overview on micro- and nanomechanical testing: New insights in interface plasticity and fracture at small length scales, Acta Materialia, 142 (2018) 248-282. doi: 10.1016/j.actamat.2017.06.019.

[3] W.C. Oliver, G.M. Pharr, An Improved Technique for Determining Hardness and Elastic-Modulus Using Load and Displacement Sensing Indentation Experiments, Journal of Materials Research, 7 (1992) 1564-1583.

[4] M.D. Uchic, D.M. Dimiduk, J.N. Florando, W.D. Nix, Sample Dimensions Influence Strength and Crystal Plasticity, Science, 305 (2004) 986-989. doi: 10.1126/science.1098993.

[5] Y. Zou, Nanomechanical studies of high-entropy alloys, J. Mater. Res., (2018) 1-20. doi: 10.1557/jmr.2018.155.

[6] H. Zhang, B.E. Schuster, Q. Wei, K.T. Ramesh, The design of accurate micro-compression experiments, Scripta Materialia, 54 (2006) 181-186. doi: 10.1016/j.scriptamat.2005.06.043.

[7] R.S. Mishra, Z.Y. Ma, Friction stir welding and processing, Materials Science and Engineering: R: Reports, 50 (2005) 1-78. doi: 10.1016/j.mser.2005.07.001.

[8] P.G. Slade, Electrical Contacts: Principles and Applications, Taylor & Francis, 1999.

[9] W. Zhou, L. Liu, B. Li, Q. Song, P. Wu, Structural, Elastic, and Electronic Properties of Al-Cu Intermetallics from First-Principles Calculations, Journal of Electronic Materials, 38 (2008) 356-364. doi: 10.1007/s11664-008-0587-0.

[10] M. Braunovic, N. Aleksandrov, Effect of electrical current on the morphology and kinetics of formation of intermetallic phases in bimetallic aluminum-copper joints, 1993.

[11] E.R. Waliach, G.J. Davies, Mechanical properties of aluminium-copper solid-phase welds, Metals Technology, 4 (2013) 183-190. doi: 10.1179/030716977803292024.

[12] T. Chanda, G.S. Murty, Plastic behaviour of CuAl2, Journal of Materials Science, 27 (1992) 5931-5934. doi: 10.1007/BF01119763.

[13] B.N. Dey, W.R. Tyson, Plastic deformation of CuAl2, physica status solidi (a), 9 (1972) 215-221. doi: 10.1002/pssa.2210090124.

[14] P. Xue, B.L. Xiao, D.R. Ni, Z.Y. Ma, Enhanced mechanical properties of friction stir welded dissimilar Al–Cu joint by intermetallic compounds, Materials Science and Engineering: A, 527 (2010) 5723-5727. doi: 10.1016/j.msea.2010.05.061.

[15] C.J. Hsu, P.W. Kao, N.J. Ho, Ultrafine-grained Al–Al2Cu composite produced in situ by friction stir processing, Scripta Materialia, 53 (2005) 341-345. doi: 10.1016/j.scriptamat.2005.04.006.

[16] H. Chen, L. Yang, J. Long, First-principles investigation of the elastic, Vickers hardness and thermodynamic properties of Al–Cu intermetallic compounds, Superlattices and Microstructures, 79 (2015) 156-165. doi: 10.1016/j.spmi.2014.11.005.

[17] D.M. Rabkin, V.R. Ryabov, A.V. Lozovskaya, V.A. Dovzhenko, Preparation and properties of copper-aluminum intermetallic compounds, Soviet Powder Metallurgy and Metal Ceramics, 9 (1970) 695-700. doi: 10.1007/BF00803820.

[18] C.L. Bauer, G.G. Lessmann, Metal-Joining Methods, Annual Review of Materials Science, 6 (1976) 361-387. doi: 10.1146/annurev.ms.06.080176.002045.

[19] R.S. Timsit, Electrical Contact Resistance: Fundamental Principles, in: P.G. Slade (Ed.) Electrical Contacts: Principles and Applications, Dekker, 1999, pp. 1-88.

[20] M.H.M. Kouters, G.H.M. Gubbels, O. Dos Santos Ferreira, Characterization of intermetallic compounds in Cu–Al ball bonds: Mechanical properties, interface delamination and thermal conductivity, Microelectronics Reliability, 53 (2013) 1068-1075. doi: 10.1016/j.microrel.2013.02.020.

[21] M. Braunovic, L. Rodrigue, D. Gagnon, Nanoindentation Study of Intermetallic Phases in Al-Cu Bimetallic System, in: 2008 Proceedings of the 54th IEEE Holm Conference on Electrical Contacts, 2008, pp. 270-275.

[22] C.C. Kammerer, S. Behdad, L. Zhou, F. Betancor, M. Gonzalez, B. Boesl, Y.H. Sohn, Diffusion kinetics, mechanical properties, and crystallographic characterization of intermetallic compounds in the Mg–Zn binary system, Intermetallics, 67 (2015) 145-155. doi: http://dx.doi.org/10.1016/j.intermet.2015.08.001.

[23] P.-F. Yang, Y.-S. Lai, S.-R. Jian, J. Chen, R.-S. Chen, Nanoindentation identifications of mechanical properties of Cu6Sn5, Cu3Sn, and Ni3Sn4 intermetallic compounds derived by diffusion couples, Materials Science and Engineering: A, 485 (2008) 305-310. doi: https://doi.org/10.1016/j.msea.2007.07.093.

[24] R.R. Chromik, D.N. Wang, A. Shugar, L. Limata, M.R. Notis, R.P. Vinci, Mechanical Properties of Intermetallic Compounds in the Au–Sn System, Journal of Materials Research, 20 (2005) 2161-2172. doi: 10.1557/JMR.2005.0269.

[25] S.S. Singh, E. Guo, H. Xie, N. Chawla, Mechanical properties of intermetallic inclusions in Al 7075 alloys by micropillar compression, Intermetallics, 62 (2015) 69-75. doi: 10.1016/j.intermet.2015.03.008.

[26] W. Luo, C. Kirchlechner, X. Fang, S. Brinckmann, G. Dehm, F. Stein, Influence of composition and crystal structure on the fracture toughness of NbCo 2 Laves phase studied by micro-cantilever bending tests, Materials & Design, 145 (2018) 116-121. doi: 10.1016/j.matdes.2018.02.045.

[27] A. Dubach, R. Raghavan, J. Loffler, J. Michler, U. Ramamurty, Micropillar compression studies on a bulk metallic glass in different structural states, Scripta Materialia, 60 (2009) 567-570. doi: 10.1016/j.scriptamat.2008.12.013.

[28] W.C. Oliver, G.M. Pharr, An improved technique for determining hardness and elastic modulus using load and displacement sensing indentation experiments, J. Mater. Res., 7 (1992) 1564-1583. doi: 10.1557/JMR.1992.1564.

[29] W.C. Oliver, G.M. Pharr, Measurement of hardness and elastic modulus by instrumented indentation: Advances in understanding and refinements to methodology, J. Mater. Res., 19 (2011) 3-20. doi: 10.1557/jmr.2004.19.1.3.

[30] P. Sudharshan Phani, W.C. Oliver, A critical assessment of the effect of indentation spacing on the measurement of hardness and modulus using instrumented indentation testing, Materials & Design, 164 (2019) 107563. doi: 10.1016/j.matdes.2018.107563.

[31] C.M. Lauener, L. Petho, M. Chen, Y. Xiao, J. Michler, J.M. Wheeler, Fracture of Silicon: Influence of rate, positioning accuracy, FIB machining, and elevated temperatures on toughness measured by pillar indentation splitting, Materials & Design, 142 (2018) 340-349. doi: 10.1016/j.matdes.2018.01.015.

[32] Y. Xiao, J. Wehrs, H. Ma, T. Al-Samman, S. Korte-Kerzel, M. Göken, J. Michler, R. Spolenak, J.M. Wheeler, Investigation of the deformation behavior of aluminum micropillars produced by focused ion beam machining using Ga and Xe ions, Scripta Materialia, 127 (2017) 191-194. doi: 10.1016/j.scriptamat.2016.08.028.

[33] J.M. Wheeler, J. Michler, Elevated temperature, nano-mechanical testing in situ in the scanning electron microscope, Rev Sci Instrum, 84 (2013) 045103. doi: 10.1063/1.4795829.

[34] M. Sebastiani, K.E. Johanns, E.G. Herbert, F. Carassiti, G.M. Pharr, A novel pillar indentation splitting test for measuring fracture toughness of thin ceramic coatings, Philosophical Magazine, 95 (2014) 1928-1944. doi: 10.1080/14786435.2014.913110.

[35] M. Ghidelli, M. Sebastiani, K.E. Johanns, G.M. Pharr, Effects of indenter angle on micro-scale fracture toughness measurement by pillar splitting, Journal of the American Ceramic Society, 100 (2017) 5731-5738. doi: 10.1111/jace.15093.

[36] J.L. Murray, The aluminium-copper system, International Metals Reviews, 30 (1985) 211-234. doi: 10.1179/imtr.1985.30.1.211.

[37] Y. Funamizu, K. Watanabe, Interdiffusion in the Al–Cu System, Transactions of the Japan Institute of Metals, 12 (1971) 147-152. doi: 10.2320/matertrans1960.12.147.

[38] A.C. Fischer-Cripps, Nanoindentation, 1 ed., Springer-Verlag New York, 2002.

[39] S. Korte-Kerzel, Microcompression of brittle and anisotropic crystals: recent advances and current challenges in studying plasticity in hard materials, MRS Communications, 7 (2017) 109-120. doi: 10.1557/mrc.2017.15.

[40] J. Michler, K. Wasmer, S. Meier, F. Östlund, K. Leifer, Plastic deformation of gallium arsenide micropillars under uniaxial compression at room temperature, Applied Physics Letters, 90 (2007) 043123. doi: 10.1063/1.2432277.

[41] S. Korte, W.J. Clegg, Discussion of the dependence of the effect of size on the yield stress in hard materials studied by microcompression of MgO, Philosophical Magazine, 91 (2011) 1150-1162. doi: 10.1080/14786435.2010.505179.

[42] Y. Zou, J.M. Wheeler, A.S. Sologubenko, J. Michler, W. Steurer, R. Spolenak, Bridging room-temperature and high-temperature plasticity in decagonal Al–Ni–Co quasicrystals by micro-thermomechanical testing, Philosophical Magazine, 96 (2016) 3356-3378. doi: 10.1080/14786435.2016.1234722.

[43] S. Schröders, S. Sandlöbes, C. Birke, M. Loeck, L. Peters, C. Tromas, S. Korte-Kerzel, Room temperature deformation in the Fe7Mo6 μ-Phase, International Journal of Plasticity, 108 (2018) 125-143. doi: 10.1016/j.ijplas.2018.05.002.

[44] C. Zehnder, K. Czerwinski, K.D. Molodov, S. Sandlöbes-Haut, J.S.K.L. Gibson, S. Korte-Kerzel, Plastic deformation of single crystalline C14 Mg2Ca Laves phase at room temperature, Materials Science and Engineering: A, 759 (2019) 754-761. doi: 10.1016/j.msea.2019.05.092.

[45] S.H. Oh, M. Legros, D. Kiener, G. Dehm, In situ observation of dislocation nucleation and escape in a submicrometre aluminium single crystal, Nat Mater, 8 (2009) 95-100. doi: http://www.nature.com/nmat/journal/v8/n2/suppinfo/nmat2370_S1.html.

[46] M. Ignat, F. Durand, Deformation lines on Al2Cu single crystals after creep in compression, Scripta Metallurgica, 10 (1976) 623-626. doi: https://doi.org/10.1016/0036-9748(76)90192-7.

[47] D. Chen, X.L. Ma, Local decomposition induced by dislocation motions inside tetragonal Al(2)Cu compound: slip system-dependent dynamics, Sci Rep, 3 (2013) 3157. doi: 10.1038/srep03157.

[48] C.-Y. Chen, H.-L. Chen, W.-S. Hwang, Influence of Interfacial Structure Development on the Fracture Mechanism and Bond Strength of Aluminum/Copper Bimetal Plate, MATERIALS TRANSACTIONS, 47 (2006) 1232-1239. doi: 10.2320/matertrans.47.1232.

[49] M. Sebastiani, K.E. Johanns, E.G. Herbert, G.M. Pharr, Measurement of fracture toughness by nanoindentation methods: Recent advances and future challenges, Current Opinion in Solid State and Materials Science, 19 (2015) 324-333. doi: 10.1016/j.cossms.2015.04.003.

[50] J.P. Best, J. Wehrs, M. Polyakov, M. Morstein, J. Michler, High temperature fracture toughness of ceramic coatings evaluated using micro-pillar splitting, Scripta Materialia, 162 (2019) 190-194. doi: 10.1016/j.scriptamat.2018.11.013.

[51] K. Gao, S. Li, S. Song, R. Zhang, X. Guo, H. Fu, Influences of microstructure and orientation on fracture toughness of intermetallic phase Al2Cu-based alloy under directional solidification, Fatigue & Fracture of Engineering Materials & Structures, 39 (2016) 511-520. doi: 10.1111/ffe.12388.

[52] G. Constantinides, F.J. Ulm, K. Van Vliet, On the use of nanoindentation for cementitious materials, Materials and Structures, 36 (2003) 191-196. doi: 10.1007/BF02479557.

[53] G. Constantinides, K.R. Chandran, F.-J. Ulm, K. Van Vliet, Grid indentation analysis of composite microstructure and mechanics: Principles and validation, Materials Science and Engineering: A, 430 (2006) 189-202.

[54] G. Constantinides, F.-J. Ulm, The nanogranular nature of C–S–H, Journal of the Mechanics and Physics of Solids, 55 (2007) 64-90. doi: 10.1016/j.jmps.2006.06.003.

[55] F.J. Ulm, M. Vandamme, C. Bobko, J. Alberto Ortega, K. Tai, C. Ortiz, Statistical indentation techniques for hydrated nanocomposites: concrete, bone, and shale, Journal of the American Ceramic Society, 90 (2007) 2677-2692.

[56] G. Constantinides, F.-J. Ulm, K. Van Vliet, On the use of nanoindentation for cementitious materials, Materials and structures, 36 (2003) 191-196.

[57] M.F. Ashby, D. Cebon, Materials selection in mechanical design, Le Journal de Physique IV, 03 (1993) C7-1-C7-9. doi: 10.1051/jp4:1993701.

[58] J.J. Vlassak, W.D. Nix, Measuring the elastic properties of anisotropic materials by means of indentation experiments, Journal of the Mechanics and Physics of Solids, 42 (1994) 1223-1245. doi: https://doi.org/10.1016/0022-5096(94)90033-7.

[59] Y. Xiao, V. Maier-Kiener, J. Michler, R. Spolenak, J.M. Wheeler, Deformation behavior of aluminum pillars produced by Xe and Ga focused ion beams: Insights from strain rate jump tests, Materials & Design, 181 (2019) 107914. doi: 10.1016/j.matdes.2019.107914.

[60] B.N. Jaya, C. Kirchlechner, G. Dehm, Can microscale fracture tests provide reliable fracture toughness values? A case study in silicon, J. Mater. Res., 30 (2015) 686-698. doi: 10.1557/jmr.2015.2.

***Highlights (for review)**

- Al—Cu intermetallic phases were investigated using combinatorial micromechanics
- Four different small-scale mechanical testing techniques are applied in this study
- Fracture results suggest superior toughness of the intermetallics
- A novel statistical map allows easy visualization of phases within property space

Figure 1

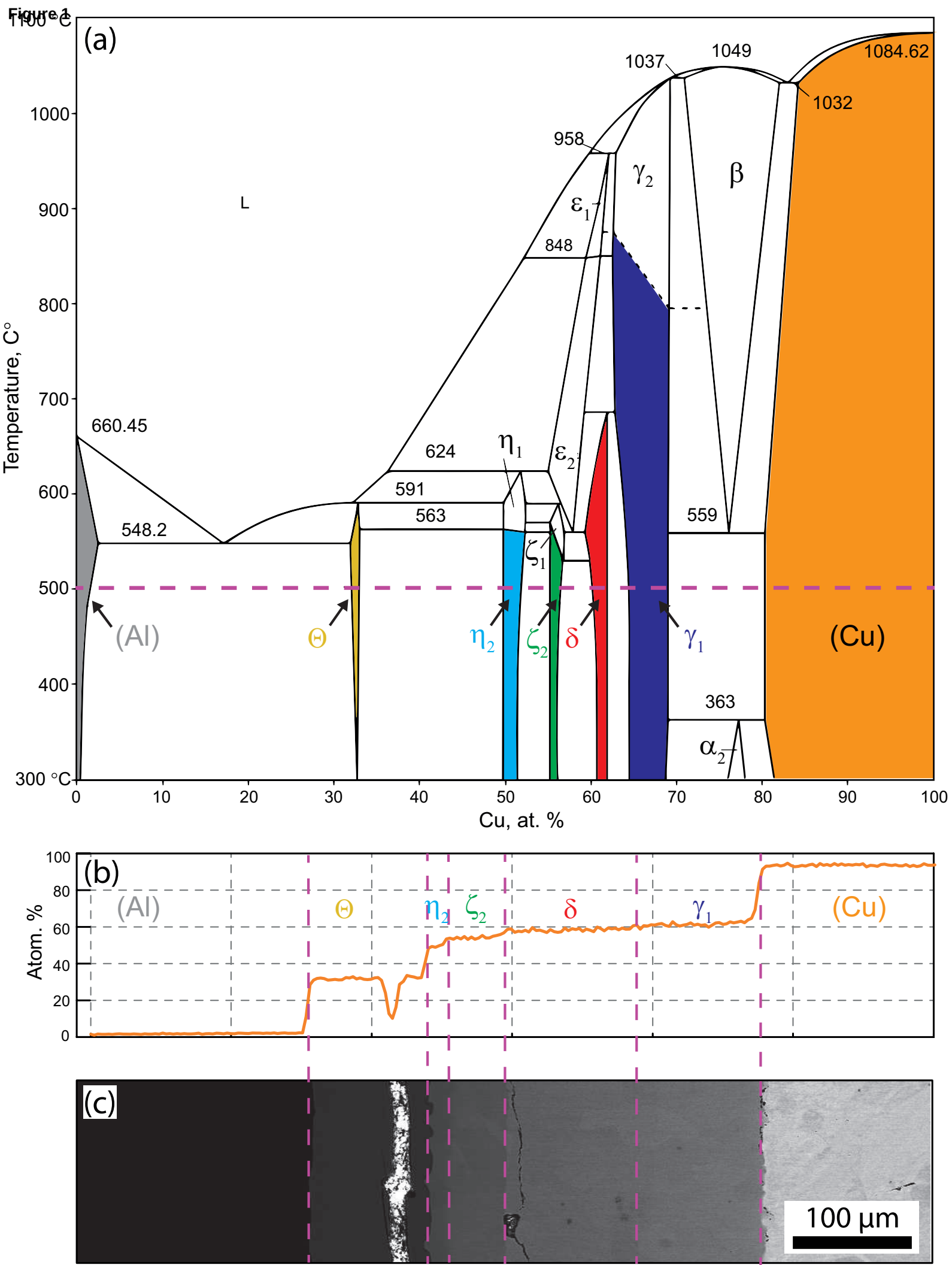
(a)
1100 °C
1000
900
800
700
600
500
400
300 °C
Temperature, C°
0
10
20
30
40
50
60
70
80
90
100
Cu, at. %
L
660.45
548.2
624
591
563
848
958
1037
1049
1084.62
1032
559
363
ε_1
γ_2
β
η_1
ε_2
ζ_1
α_2
(Al)
Θ
η_2
ζ_2
δ
γ_1
(Cu)
(b)
Atom. %
100
80
60
40
20
0
(Al)
Θ
η_2
ζ_2
δ
γ_1
(Cu)
(c)
100 µm

Figure 2

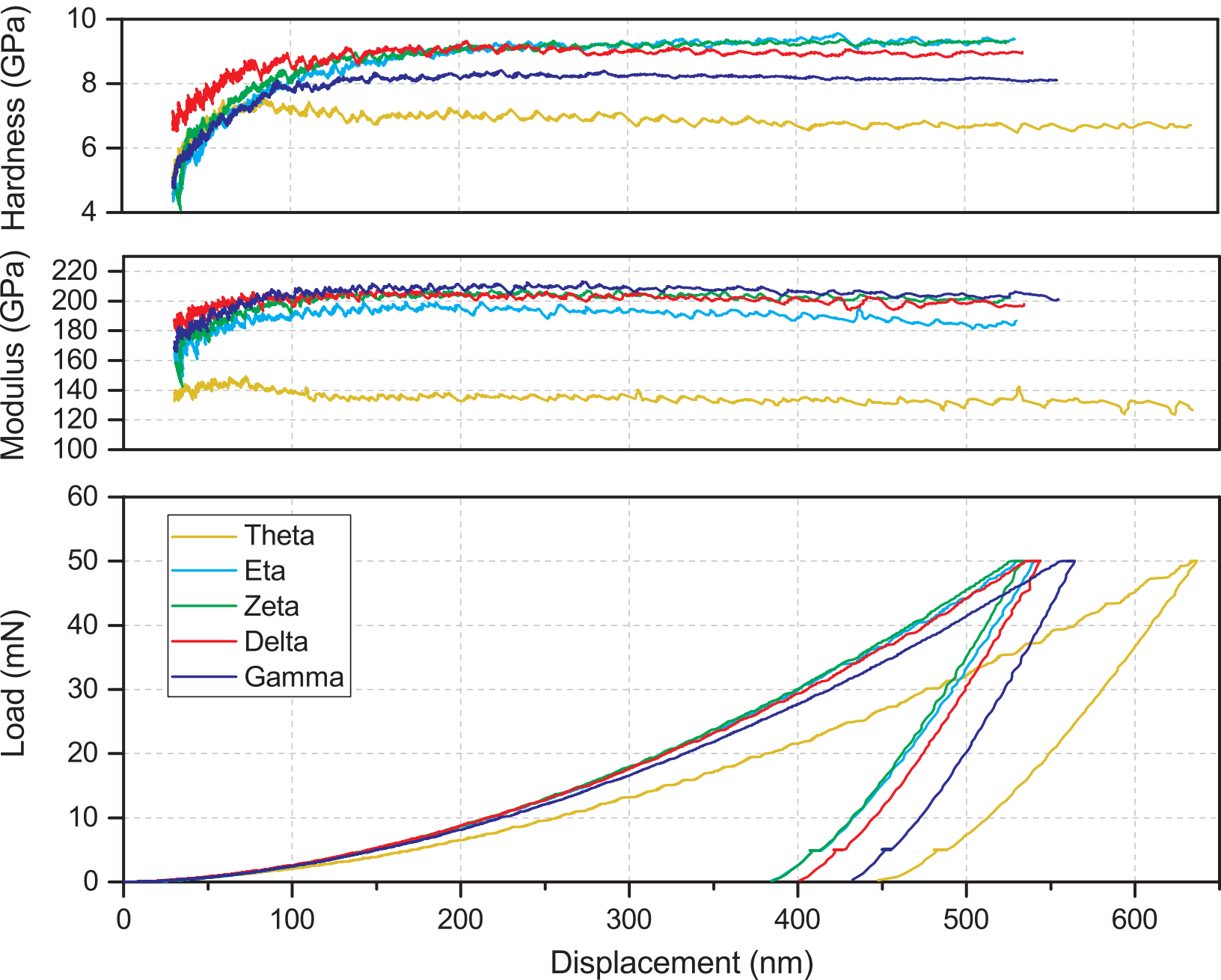
Hardness (GPa)
10
8
6
4
Modulus (GPa)
220
200
180
160
140
120
100
Load (mN)
60
50
40
30
20
10
0
Theta
Eta
Zeta
Delta
Gamma
0
100
200
300
400
500
600
Displacement (nm)

Figure 3 Θ

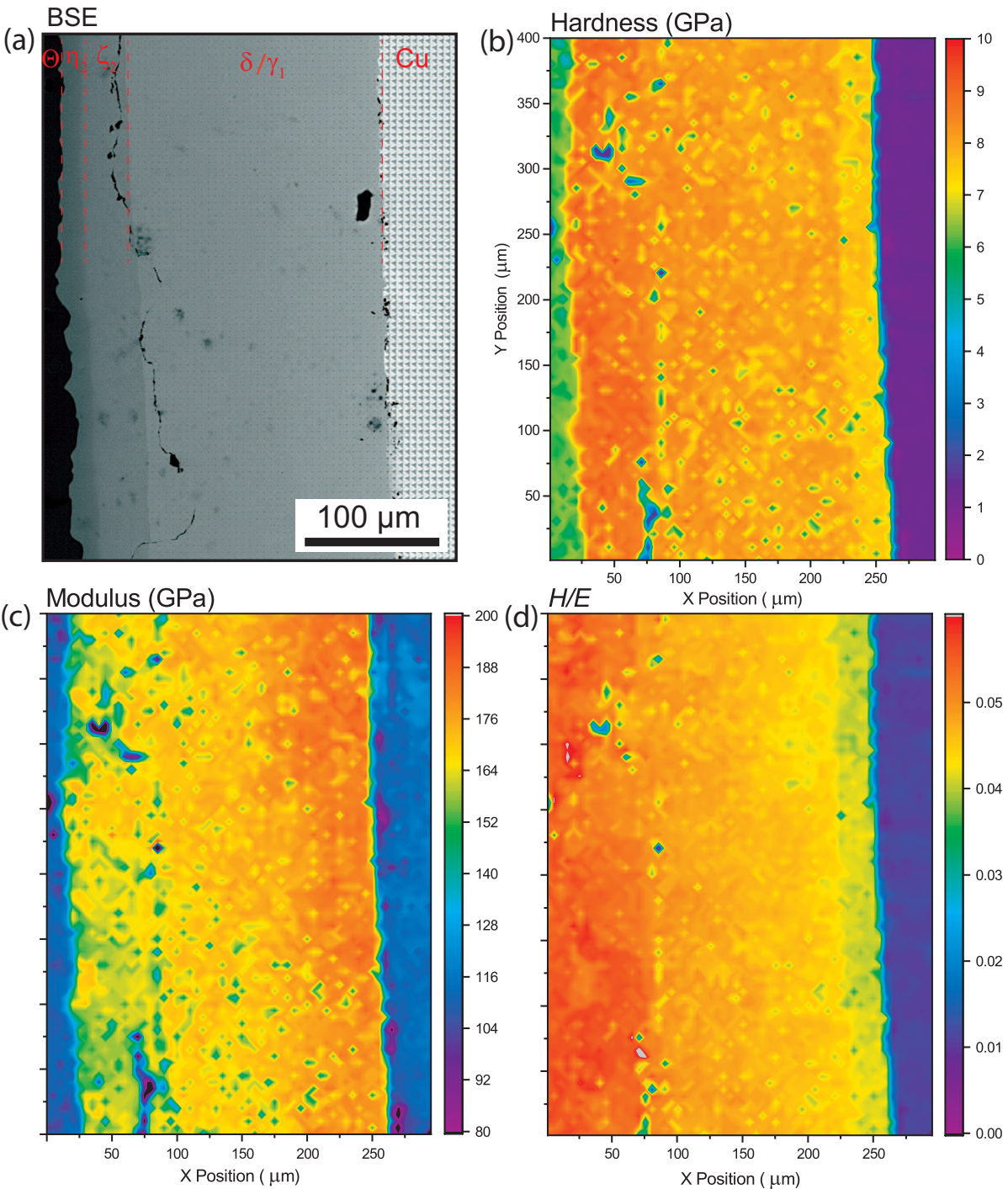
(a)
BSE
Θ
η_2 ζ_2
δ/γ_1
Cu
100 μm
(b)
Hardness (GPa)
Y Position (μm)
X Position (μm)
(c)
Modulus (GPa)
X Position (μm)
(d)
H/E
X Position (μm)

Figure 4

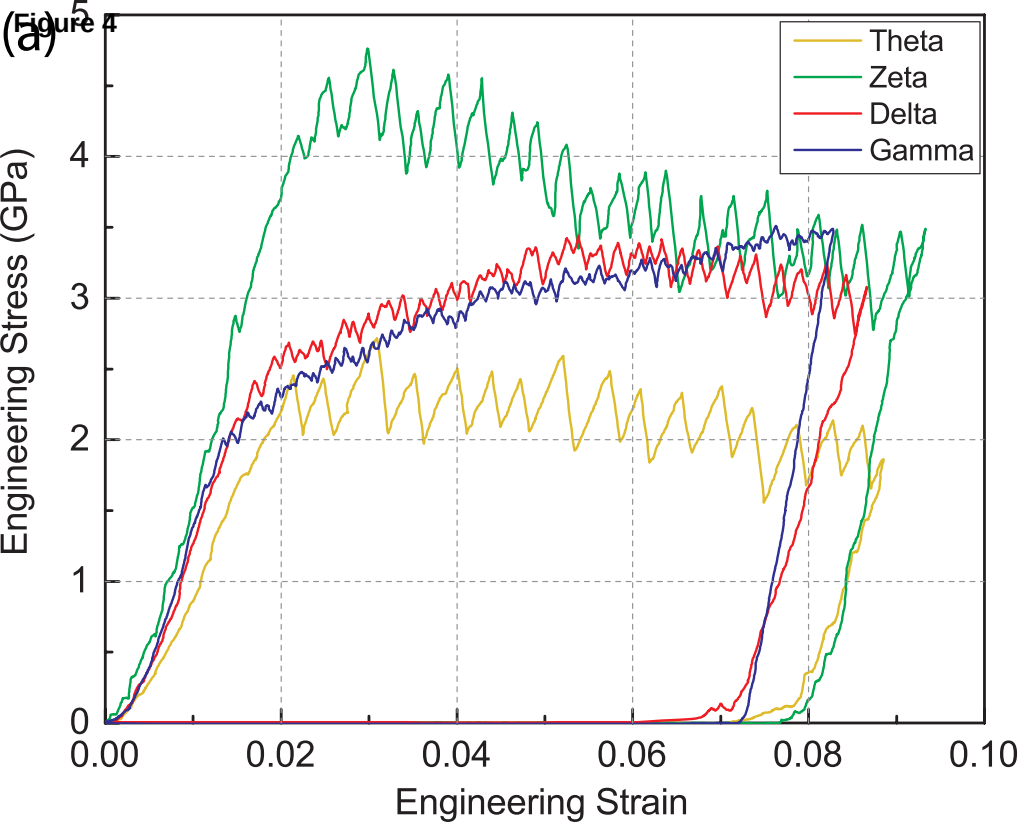
(a)
Theta
Zeta
Delta
Gamma
Engineering Stress (GPa)
Engineering Strain
0
1
2
3
4
5
0.00
0.02
0.04
0.06
0.08
0.10

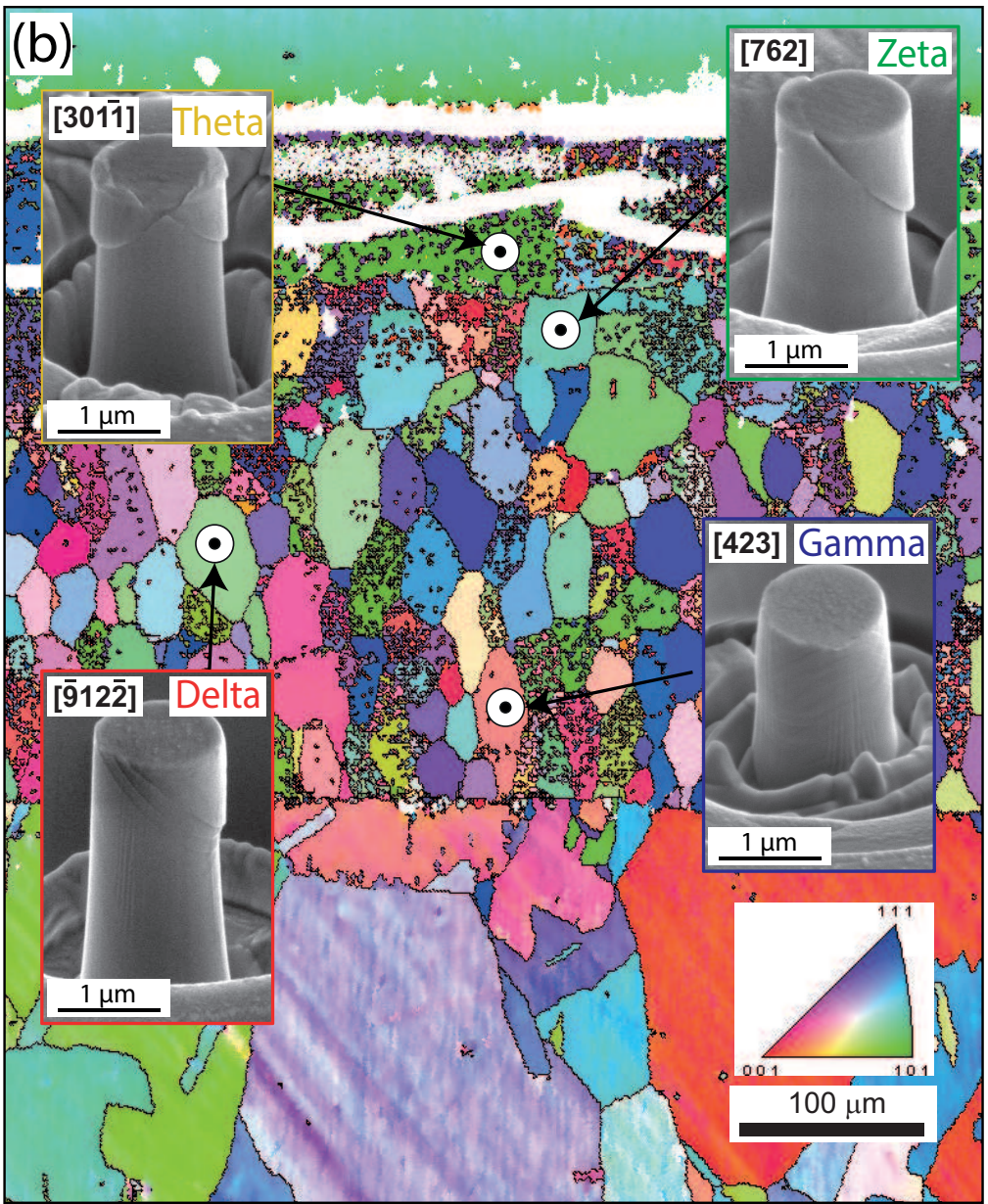
(b)
[30$\bar{1}\bar{1}$]
Theta
1 µm
[762]
Zeta
1 µm
[423]
Gamma
1 µm
[$\bar{9}12\bar{2}$]
Delta
1 µm
111
001
101
100 µm

Figure 5

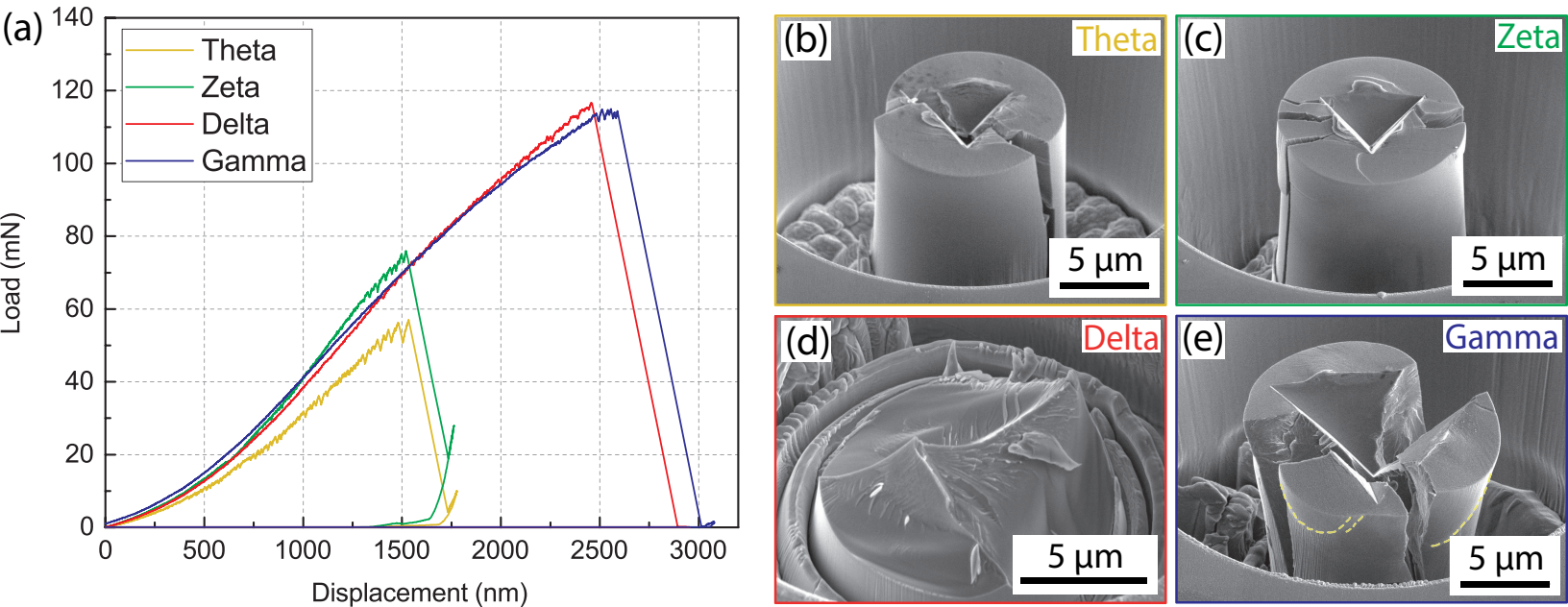
(a)
Theta
Zeta
Delta
Gamma
Load (mN)
Displacement (nm)
0
20
40
60
80
100
120
140
0
500
1000
1500
2000
2500
3000
(b)
Theta
5 µm
(c)
Zeta
5 µm
(d)
Delta
5 µm
(e)
Gamma
5 µm

Figure 6

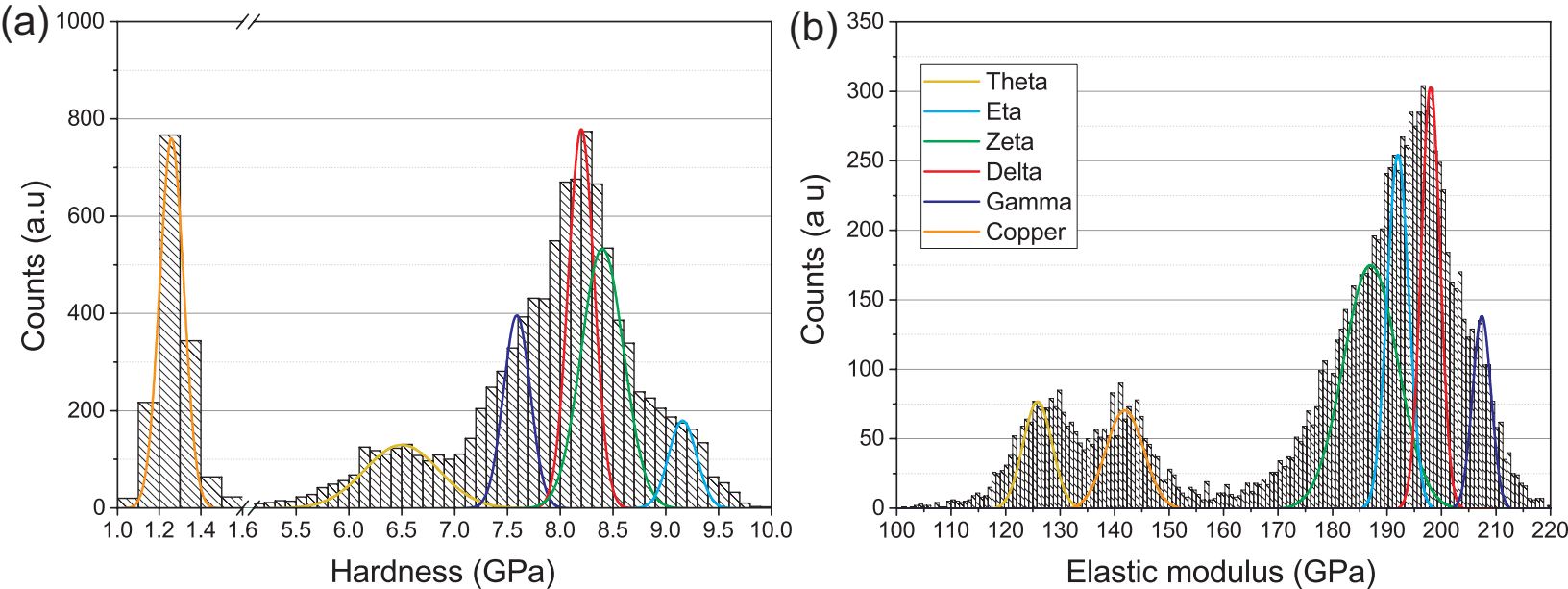
(a)
Counts (a.u)
Hardness (GPa)
1000
800
600
400
200
0
1.0 1.2 1.4 1.6 5.5 6.0 6.5 7.0 7.5 8.0 8.5 9.0 9.5 10.0
(b)
Counts (a u)
Elastic modulus (GPa)
350
300
250
200
150
100
50
0
100 110 120 130 140 150 160 170 180 190 200 210 220
Theta
Eta
Zeta
Delta
Gamma
Copper

Figure 7

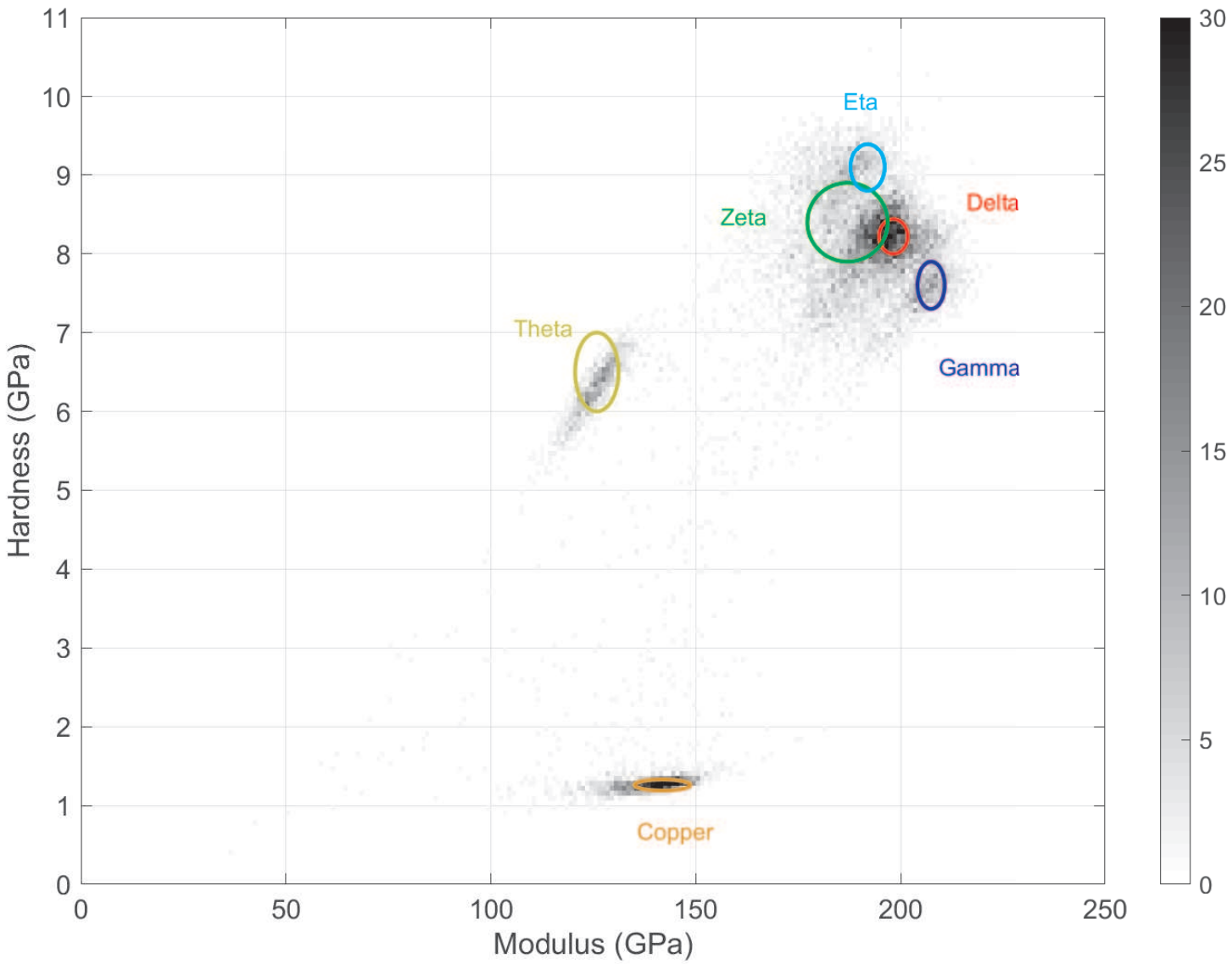
Eta
Zeta
Delta
Theta
Gamma
Copper
Hardness (GPa)
Modulus (GPa)
0
1
2
3
4
5
6
7
8
9
10
11
0
50
100
150
200
250
0
5
10
15
20
25
30

Figure 8

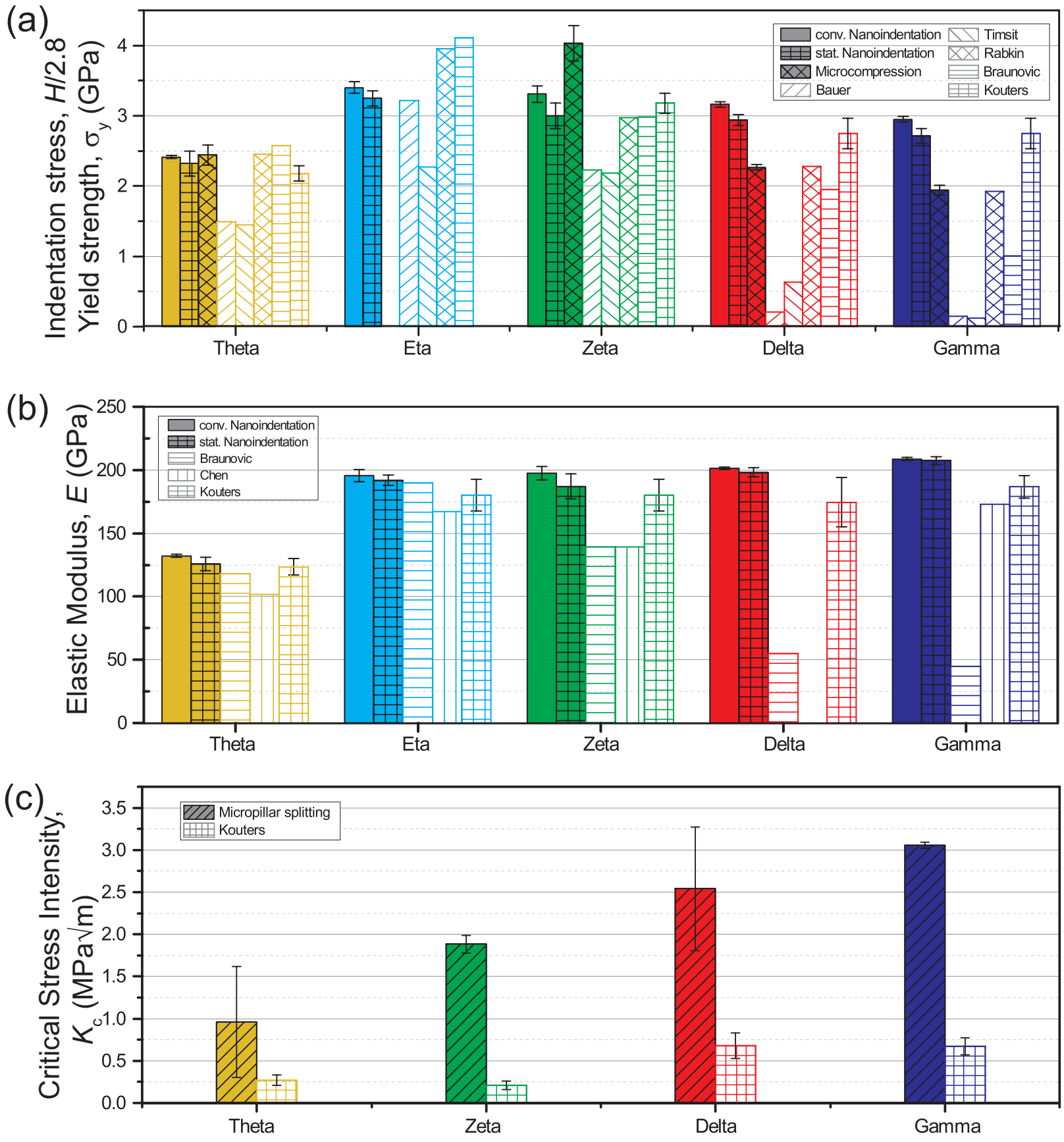
(a)
Indentation stress, H/2.8
Yield strength, σy (GPa)
0
1
2
3
4
Theta
Eta
Zeta
Delta
Gamma
conv. Nanoindentation
stat. Nanoindentation
Microcompression
Bauer
Timsit
Rabkin
Braunovic
Kouters
(b)
Elastic Modulus, E (GPa)
0
50
100
150
200
250
Theta
Eta
Zeta
Delta
Gamma
conv. Nanoindentation
stat. Nanoindentation
Braunovic
Chen
Kouters
(c)
Critical Stress Intensity, Kc (MPa√m)
0.0
0.5
1.0
1.5
2.0
2.5
3.0
3.5
Theta
Zeta
Delta
Gamma
Micropillar splitting
Kouters

*Declaration of Interest Statement

The authors declare no competing financial interest.

***Author Contributions Section**

Y. Xiao: Conceptualization, Investigation, Writing - original draft, Writing - review & editing. H. Besharatloo: Investigation, Writing - review & editing. B. Gan: Resources, Writing - review & editing. B. Gan: Resources, Writing - review & editing. X. Maeder: Investigation, Writing - review & editing. J.M. Wheeler: Conceptualization, Supervision, Writing - review & editing.